Enhancing the translational potential of photo-responsive covellite in medicine: solvent-free tuning of CuS nanoparticles LSPR and control of their stability in aqueous media by a

Materials Today Chemistry 46 (2025) 102765

Contents lists available at ScienceDirect

Materials Today Chemistry

journal homepage: www.journals.elsevier.com/materials-today-chemistry/

Enhancing the translational potential of photo-responsive covellite in medicine: solvent-free tuning of CuS nanoparticles LSPR and control of their stability in aqueous media by a carbonaceous shell

Sathish Shanmugam [a,1], Francesco Barbero [a,1], Aurora Bellone [b], Alessia Giovanna Santa Banche Niclot [c], Simone Miatto [a], Guido Perrone [b], Katia Mareschi [c,d], Ivana Fenoglio [a,*]

[a] Department of Chemistry, University of Torino, Torino, Italy
[b] Department of Electronics and Telecommunications, Politecnico di Torino, Torino, Italy
[c] Cellular Therapy Laboratory, Paediatric Onco - Haematology Division, Regina Margherita Children's Hospital, City of Health and Science of Turin, Torino, Italy
[d] Department of Public Health and Paediatrics, University of Turin, Italy and Stem Cell Transplantation, Turin, Piedmont, Italy

ARTICLE INFO

Keywords:
Photothermal therapy
Copper sulfide NPs
Carbon coating
Mesenchymal stem cells

ABSTRACT

Covellite (CuS) nanoparticles (NPs) are versatile, non-noble metal plasmonic materials which have been recognized as promising candidates for therapeutical applications. However, the poor chemical stability of CuS NPs in aqueous media makes their use in medical applications challenging. While the application of coatings to reduce NPs degradation has been successfully proposed for other materials, in the case of CuS this strategy is limited by the loss of the plasmonic performance due to NPs chemical instability in the post-synthesis treatments. In the present study, we successfully obtained core-shell CuS@C nanocomposites with tailored size, enhanced stability, and superior photothermal performance, by applying a novel green synthetic strategy using water as solvent. CuS NPs were synthetized using polyvinylpyrrolidone (PVP) as stabilizer; in addition, a PVP concentration-dependent tunability of size and plasmon wavelength was demonstrated. The carbon shell was generated via hydrothermal carbonization without compromising the plasmonic performance of CuS NPs (52 % of photothermal conversion efficiency) and without inducing aggregation through a strict control of the dissolution/degradation process. The carbon coating slowed down the degradation of CuS NPs in biological fluids without inhibiting the redox activity evaluated as a generation of hydroxyl radicals by electron paramagnetic resonance spectroscopy. When tested in vitro for their cytotoxicity toward mesenchymal stem cells CuS@C appear non cytotoxic after 24 h of incubation up to 100 μg/mL. Moreover, the carbon shell inhibited the pro-proliferative effect observed for CuS NPs at low concentration after 48 h. Overall, the results prove the great potential of CuS@C nanocomposites as photothermal agents for cancer treatments.

1. Introduction

Noble metal Au and Ag nanoparticles (NPs), represent so far, the most intensively studied class of plasmonic materials for a range of biomedical applications such as cancer therapy, bio-imaging and sensing [1–5]. However, over the past decade, an incessantly interest has been growing in searching for alternative plasmonic materials consisting of earth-abundant non-noble metal elements, aiming at further enhancing plasmonic performance while mitigating cost issues for real-world applications [6–8]. For this purpose, a variety of semiconductor materials, such as metal oxides [9–12], chalcogenides [13–17], phosphides [18,19] and nitrides [20,21] have been investigated for their metal-like plasmonic features. Copper sulfide is a *P*-type semiconductor, recently recognized as a versatile non-noble metal plasmonic material. It has attracted much attention of researchers due to dual-functionality: it integrates excitonic properties of semiconductors with metal like plasmonic behaviors, exhibiting the localized surface plasmon resonance (LSPR) in the near infrared region (NIR) [22,23].

* Corresponding author.
E-mail address: ivana.fenoglio@unito.it (I. Fenoglio).
[1] These authors contributed equally to this work.

https://doi.org/10.1016/j.mtchem.2025.102765
Received 26 February 2025; Received in revised form 30 April 2025; Accepted 15 May 2025
Available online 20 May 2025

Due to this dual functionality, copper sulfide NPs becomes as a potential candidate in many fields such as optoelectronics, photocatalysis, photovoltaic cells, sensors, battery electrodes manufacturing and in medicine [24–27]. In contrast to the metallic materials whose plasmonic behavior is due to the delocalized conduction electrons, the LSPR in copper sulfides semiconductor NPs arises from the collective oscillation of free holes in their valence bands [23,28]. The structure, band gap and plasmonic properties of copper sulfides ($Cu_{2-x}S$) compounds can be altered by varying their stoichiometries. The stoichiometric factor (2-x) in $Cu_{2-x}S$ varies in a wide range between 1 and 2 and thereby it leads to formation of the Cu-rich chalcocite (Cu_2S) to Cu deficient covellite (CuS) crystal structure [17,29,30]. The latter phase exhibits intrinsic plasmonic characteristics due to its high free hole concentration ($\sim 10^{22}$ cm^{-3}) [31,32] while the chalcocite phase is plasmonically inactive due to the lack of free holes in its valence band [28]. $Cu_{2-x}S$-based NPs have attracted a high interest in medicine as antibacterial agent and in tumors therapy. In fact, the ability to convert NIR light into heat makes them efficient photothermal agents (PTA) [33,34].

Photothermal therapy (PTT) consists of exposing the tumor site to extremely high temperatures (above 45 °C) for a short time, causing thermal ablation and consequent cell death, or maintaining temperatures between 42 °C and 43 °C to induce cellular damage and increase the permeability of tumor arteries [35,36]. Such a temperature increase is usually achieved by exploiting PTA that can convert light energy into heat. PTA activated by NIR range of the spectrum are particularly interesting since the human tissue is "transparent" to photons at this energy level [37]. Therefore, NIR radiation penetrates deeper than visible light in biological tissues, allowing for a subcutaneous tumor treatment. Nanomaterials with absorbance window at NIR region, high photothermal conversion efficiency, good photothermal stability and tunable properties are ideal candidates for PTT. In this regard, CuS NPs has been considered as a good PTA since it possesses the above-mentioned features [32]. Furthermore, in comparison to Au NPs, CuS has an advantage of easy and simple preparation. In fact, Au rods and bipyramid, which are the only gold nanostructures absorbing NIR wavelength, require complex synthesis and the highly toxic cationic surfactant cetyltrimethylammonium bromide (CTAB), which can be removed only following additional post-synthesis treatments [38]. Further, the reproducibility of the synthesis of this gold nanostructures are not straightforward. Another peculiarity of CuS NPs is the ability to generate cytotoxic reactive oxygen species (ROS) and copper ions. These species act synergically to heat, enhancing the efficacy in inducing cell death [39,40].

Despite the increasing interest, the development of CuS-based nanomaterials for biomedical application is still at a pre-clinical stage due to some important drawbacks. Most of the syntheses of copper sulfide NPs have been realized using heating-up or hot-injection approach in organic media, resulting in materials incompatible with aqueous media. Moreover, the proposed syntheses are often expensive and performed with toxic reagents [33]. In order to obtain aqueous colloidal formulation for medical applications, post-synthetic ligand exchange is needed, which complicates the whole preparation process often leading to undesired alterations of the optical properties of the resulting NPs and more specifically, shifting and damping of their LSPR property [41]. Direct aqueous synthesis is obviously a more straightforward approach and environmentally friendly process than synthesis in organic media. Alternative ways to obtain hydrophilic copper sulfides NPs in an aqueous medium have been previously developed [42,43]. However, compared to the synthesis in organic media there is very poor control over the size and morphology of the resulting nanocrystals and consequently, the LSPR tuning of CuS NPs in aqueous medium is still a challenge. Moreover, the very poor chemical stability in the aqueous environment of CuS NPs limits several synthetic strategies. The stability of CuS NPs in an aqueous environment is also an important aspect to ensure their usage in the medical field. While dissolution facilitates the clearance of NPs from the body after the treatment, an advantage with respect to highly persistent gold NPs [44] it should be slow enough in the target tissue to allow for the PTT treatment. One possible strategy to control the NPs dissolution rate is the application of coatings on NPs surface. Recent studies from our group proved that carbon coating can effectively prevent the dissolution of iron oxide nanoparticles, improving NPs stability and biocompatibility [45]. However, previous studies show that LSPR performance of CuS NPs is remarkably lost during coating with inorganic or organic materials [46,47].

In the present study the synthesis of CuS@C nanocomposites having tailored size, enhanced stability and high photothermal performance by using a green hydrothermal method in aqueous medium is reported. A deep investigation on the role of synthetic parameters on the NPs properties allowed to finely tune the size avoiding aggregation. The stability of these NPs in biological fluids, their ability to generate ROS and their cytotoxicity toward mesenchymal stem cells (MSCs) were evaluated. Overall, the results prove the great potential of CuS@C nanocomposites, laying the foundation for their future use in NIR-triggered cancer treatments.

2. Materials and methods

2.1. Chemicals

Copper (II) nitrate [$Cu(NO_3)_2$ $2.5H_2O$] (≥99.99 % USA), sodium sulfide (Na_2S $9H_2O$) (≥98.0 % India), polyvinylpyrrolidone (PVP) molecular weight = 55000 Da, sodium carbonate ($Na_2CO_3.10H_2O$) (≥99.5 % Germany), sodium bi carbonate (≥99.5 % USA), sodium L-tartrate dibasic dihydrate (≥99.99 % USA), sodium hydroxide (≥99.5 % USA), L-ascorbic acid (≥99 % China), D-Glucose (≥99 % Germany), L-Cysteine (98 % USA) were purchased from Sigma-Aldrich and Bicinchoninic acid (BCA) was purchased from Alfa Aesar, (USA); Ultrapure water was obtained by a Millipore milli-Q system.

2.2. Synthesis of CuS nanoparticles

The CuS nanoparticles synthesis has been set-up starting from a method previously reported with some modification [48]. Briefly, an appropriate amount of PVP was completely dissolved in 58 mL of Milli-Q water, then 1 mL of 60 mM $Cu(NO_3)_2$ aqueous solution was added under constant stirring. The temperature of Cu-PVP solution increased to 100 °C. After 3 min of boiling, 1 mL of 60 mM Na_2S was injected into Cu-PVP solution. The resulting CuS NPs suspension was immediately cooled down and purified by multiple washing with water by ultra-centrifugation (2500g, 5 min or 15 min depending upon PVP concentration) using an Amicon Ultra-15 filter unit (Millipore) and stored at 4 °C.

2.3. Synthesis of carbon coated CuS nanoparticles

An appropriate amount of glucose was added into 1 mM concentrated colloidal CuS nanoparticles suspension, and the required quantity of S source (Na_2S or cysteine) was added with constant stirring. Then the resultant solution was transferred into in a Teflon-lined stainless-steel autoclave (100 ml, Büchi AG) and placed in a preheated oven (190 °C) for 3 h for completion of the reaction then allowed to cool naturally. CuS@C nanoparticles were purified by multiple washing with water by ultra-centrifugation (2500g and 5 min) using an Amicon Ultra-15 filter unit (Millipore) and stored at 4 °C. As a control, hydrothermal synthesis was also performed without the addition of the S source.

2.4. Nanoparticles characterization

Powder X-ray diffraction (XRD) analysis was performed using a X'Pert PRO MPD (PANalytical) X-ray diffractometer equipped with Cu Kα radiation, configured in capillary mode over the 2θ range of 20–70°. Phase identification was performed using the X'Pert High-Score

software. The nanoparticles suspension was air-dried at 60 °C before analysis. For optical analysis, UV–Vis–NIR absorbance spectra were recorded on the colloidal suspension by a spectrophotometer (UV-Vis-NIRCary 5000, Agilent). The morphological analysis was performed by High Resolution Transmission Electron Microscopy (HRTEM, FEI-Tecnai F30 microscope at a working voltage of 300 KV). A droplet of the suspension was added to a TEM holey carbon grid (copper mesh support). Once the solvent evaporated, the material remained on the grid for analysis. TEM images were obtained with a coupled CCD camera (Gatan). The X50 (median), the mean size distribution of the particles, the standard deviation referred to the particles distribution width and shell thickness were evaluated on at least 270 particles by ImageJ software measured in at least four different regions of the TEM grid, the measurements were performed in triplicates to determine the mean absolute errors (measurement precision). The NPs sizes are reported as median (X50) and mean size of the particle distribution ± the mean absolute errors. Moreover, are reported the standard deviation as width of the distribution (SD) and the number of particles measured on the TEM images (counts).

The hydrodynamic size distributions were measured by dynamic light scattering (DLS). The DLS measurements were performed using a Malvern Zetasizer Nano ZS instrument (Malvern Panalytical Ltd, UK), equipped with a light source wavelength of 632.8 nm; 3 replicates; setting measurement angle = 173 °C, temperature = 25 °C and equilibration time = 120 s. The parameters used for the NPs were as follows: refractive index = 2.420; and absorption = 1.00. The parameters used for the water dispersant were as follows: refractive index = 1.330; viscosity (25 °C) = 0.8872 cP; and dielectric constant = 78.5. Measurements were performed on 0.5 mM concentrated solution at 6.2 pH. The results were expressed as mean values of 3 independent measurements and the diameters were reported as distribution by intensity calculated by non-negative least squares analysis. Z-potentials were measured using the electrophoretic light scattering analyser (Zetasizer Nano ZS, Malvern). FT-IR spectra of precipitated powders were recorded using a PerkinElmer Spectrum Two FT-IR Spectrometer equipped with a universal attenuated total reflection (UATR) module performing 16 scan per sample.

2.5. Chemical stability test on CuS and CuS@C NPs

CuS and CuS@C NPs (0.5 mM) samples were incubated in water under different temperatures (4 and 37 °C) and pH values [pH 1.3, pH 4.5 phosphate buffer (PB), pH 5.3 pH 6.0, pH 11], in phosphate buffer saline (PBS) (pH 7.4; PB: 10 mM, NaCl: 0.137 M), The pH values were adjusted to the desired level using HCl or NaOH solutions. The test was also performed in Dulbecco's Modified Eagle Medium [DMEM, (Invitrogen Life Technologies, Carlsbad, CA) supplemented with 10 % fetal bovine serum (FBS)]. The dissolution of the NPs was assessed by measuring the absorption of the plasmonic peak by UV–vis–NIR analysis. Furthermore, the release of Cu^{2+} ions from the degradation of CuS and CuS@C NPs were quantified by bicinchoninic acid (BCA) assay using UV–Visible spectrophotometer. The BCA assay solution was prepared by dissolving 0.5 g of bicinchoninic acid, 2.8 g of $Na_2CO_3{\cdot}10H_2O$, 0.08 g of sodium tartrate dihydrate, 0.28 g of $NaHCO_3$ and 50 mg of NaOH into 50 mL of Milli-Q water. The pH of the solution was 10.3 (target working range of pH 9.4–11.2). After incubation the particles were separated by ultra-centrifugation using Amicon Ultra-15 membrane filter and the filtrated solution was used for copper ions quantification test. For BCA test, 500 μL of BCA assay solution was added to 500 μL filtrated solution and then 100 μL of 40 mM ascorbic acid was added. After 3 min, the absorbance value at 562 nm was recorded. The concentration of copper ions was determined by a calibration curve obtained using known concentration solutions of $Cu(NO_3)_2$.

2.6. Digestion and quantification of CuS and CuS@C NPs

In order to quantify the yield of the reaction, the prepared CuS and CuS@C NPs were completely digested and the Cu^{2+} ions present in the samples were quantified by above mentioned BCA assay test. For complete digestion, NPs were incubated at 42 °C for 48 h in acidic pH (using 1 M HCl with volume ratio from 10 % to 90 %). The sample incubated using 10 % HCl solution alone gave a satisfactory result due to restriction of BCA assay working pH windows (basic buffer solution). The Cu^{2+} ions concentration in precursor solution (Cu-PVP solution used in synthesis) was verified by BCA test. After completion of the synthesis, the Cu^{2+} ions concentration in the unpurified sample solution was evaluated after digesting the CuS NPs present in the solution and this value was highly coinciding with the amount of Cu^{2+} ions in the precursor solution which validates our digestion protocol. Cu^{2+} ions concentration in unpurified solution was assumed as 100 % and the quantum yield of reaction was quantified as 70 % on purified sample.

2.7. Calculation of free carrier (hole) density in the as-synthesized CuS NPs

According to the Drude model, the frequency ω_{LSPR} of the localized surface plasmon resonance can be described as [28,30]:

$$\omega_{LSPR} = \sqrt{\frac{\omega_p^2}{1 + 2\varepsilon_m} - \gamma^2}$$

In the expression above, γ is the linewidth of the plasmon resonance band, ε_m represents the optical dielectric constant of the medium surrounding the NPs ($\varepsilon_m = 1.8$ for water) [49] and ω_P is the plasma frequency. Since ω_{LSPR} and γ are known from the experimental spectrum (see Fig. S4), corresponding ω_P values for CuS NPs prepared using different concentration of PVP have been calculated (see table 1 in SI). The relationship between bulk plasma frequency (ω_p) and free carrier density (N_h) is:

$$\omega_p = \sqrt{\frac{N_h e^2}{\varepsilon_0 m_h}}$$

where m_h is the hole effective mass, approximately 0.8 m_0 (where m_0 is the electron mass), and e is the electron charge. Using the above equation, we estimated the N_h for the as-synthesized covellite CuS NPs (see table 1 in SI).

2.8. Photo-thermal properties

For measuring the temperature change mediated by prepared samples, 3 mL of CuS nanoparticles (100 μg/mL) or CuS@C (equal to 100 μg/mL of CuS) in water were irradiated using a collimated beam emitted by a fiber-coupled 915 nm high-power laser diode. In the experimental setup, two power conditions were used by operating the diode laser at driving currents of 1.5 A and 3.5 A, corresponding to low and high power density regimes, respectively. The laser beam, emitted from the delivery fiber, was collimated using a plano-convex lens designed for the infrared spectral range (focal length: 50 mm; Thorlabs LA4148-B). This lens was mounted within a collimation tube, which was precisely aligned with the sensor of a commercial power meter (LaserPoint LPT-PLUS-2.0-USB) to measure the output power for the two current settings.

Following power measurement, the power meter was replaced by a cuvette containing the NPs dispersions. Based on the optical alignment and the geometry of the system, it was determined that approximately 80 % of the total measured power effectively irradiated the cuvette. This translated into actual power densities of 650 mW/cm^2 for the low-power condition and 2360 mW/cm^2 for the high-power condition. These two power densities, 650 mW/cm^2 and 2360 mW/cm^2 were considered during the tests. To calculate the photo-thermal conversion efficiency,

the particles were continuously irradiated until steady state temperature was reached; then the system was allowed to cool down naturally. In order to investigate the photo-stability of the CuS@C NPs, a solution containing the nanoparticles was irradiated with the same 915 nm NIR laser diode at the higher power density (2360 mW/cm^2) for 5 min (laser on), followed by naturally cooling down to room temperature without laser irradiation (laser off) for three cycles. The temperature changes in the solution were measured using fiber Bragg grating (FBG) based sensors. Fiber Bragg gratings are in-fiber components fabricated by inducing a periodic modulation in the refractive index of the fiber core. This modulation creates a notch-like spectral response in which a specific wavelength, the Bragg wavelength, is reflected when the fiber is illuminated with a broadband light source. Since the Bragg wavelength is sensitive to temperature and strain, its variation can be exploited as a thermometer for temperature sensing. The main advantage of this approach is that FBGs are not affected by self-heating artifacts induced by laser light, a common issue in conventional electrical sensors. For the experimental activities, the FBGs were fabricated in-house at Politecnico di Torino using a femtosecond laser machine. The high energy laser beam precisely modifies the core's refractive index in a localized spot to achieve the desired Bragg wavelength. The FBGs employed in the activity are 2 mm long and were interrogated using the commercial Luna's HYPERION si155 system.

2.9. Calculation of photothermal conversion efficiency

3 mL of 100 μg/mL of CuS and CuS@C NPs solution was loaded into a cuvette and irradiated using a 915-nm laser until steady state temperature was reached, followed by natural cooling after the laser was turned off. The monitored temperature profile is shown in Fig. 5A. The photothermal conversion efficiency (η) is calculated by modified Roper methods [50] according to the following equation [51,52].

$$\eta = \frac{\mathbf{mc}\left(\mathbf{T_{max}} - \mathbf{T_{max,H2O}}\right)}{\mathbf{I}\left(\mathbf{1} - \mathbf{10}^{-\mathbf{A}}\right)\boldsymbol{\tau}_{\mathbf{s}}}$$

where m is the solution mass and equal to 3.0 g (since 3 mL of solution has been used for the current study), c is the heat capacity of water and equal to 4.2 J/g, T_{max} is the maximum temperatures reached for the nanoparticle solution which are 28.97 °C for CuS and 29.85 °C for CuS@C, T_{max}, H_2O is the maximum temperatures reached for water which is 21.5 °C, I is the laser power and equal to 650 mW/cm^2 in the current study, A is the absorbance of the nanoparticle solution at 915 nm and equal to 2.1 for CuS NPs and 2.9 for CuS@C NPs (from UV–vis–NIR spectra). τ_s is the system time constant and could be calculated by plotting -ln $\left(\frac{T-T_{env}}{T_{max}-T_{env}}\right)$ as a function of time t during the cooling phase, one obtains the value τ_s from the slope of linear fitting. The calculated τ_s value is equal to 293.2 s for CuS NPs and 312.4 s for CuS@C NPs (see Fig. SI–12). The photothermal conversion efficiency was calculated as 50 % for CuS NPs and 52 % for CuS@C NPs by using these parameters.

2.9.1. Electron paramagnetic resonance

The hydroxyl radical generation by CuS and CuS@C NPs was investigated using electron paramagnetic resonance (EPR)/spin trapping technique. 50 μL of NPs suspension (300 μM in water) and 50 μL of phosphate saline buffer (10 mM, 137 mM NaCl, pH 7.4) were taken in a cuvette and stirred in the dark. 100 μL of solution (177 mM) of 5,5-dimethyl-1-pyrroline N-oxide (DMPO) in water was added. The reaction was started by adding 50 μL of 200 mM H_2O_2. EPR spectra were measured on the suspension (Miniscope MS100, Magnettech, Berlin, Germany) and the gain was set at 500. The reaction was repeated in the absence of NPs (quantity of H_2O was added) as control. EPR spectra were measured on the NPs suspensions and in absence of NPs (negative control) after 15, 30, 45 and 60 min. The experiments have been repeated almost three times. EPR spectra also recorded for the Cu^{2+} ions released from these NPs incubated in physiological temperature for 24h and in presence of 40 mM H_2O_2 for 1h at room temperature.

2.10. Biocompatibility and reactivity of CuS NPs

To analyze the biocompatibility, reactivity, safety, and potential biomedical applications of CuS NPs, their effects on mesenchymal stem cells were studied. Three batches of bone marrow mesenchymal stromal cells (MSCs) were thawed from our pediatric MSC collection and expanded at the third passage using Dulbecco's Modified Eagle's Medium (DMEM, Sigma Aldrich, St. Louis, MO, USA) supplemented with 1 % L-glutamine, 1 % penicillin/streptomycin, and 10 % human platelet lysate (HPL) and maintained at 37 °C in a 5 % CO_2 atmosphere. These cells were isolated following established protocols, as previously described [53,54]. Human bone marrow (BM) samples were collected after obtaining written informed consent, in accordance with the Ethics Committee approved by Ospedale Infantile Regina Margherita-Sant'Anna-Ordine Mauriziano hospitals' ethics committees"(protocol number 0040314, approved on 04/07/2022) and in compliance with the Declaration of Helsinki. BM cells were harvested from unfiltered BM collection waste bags, which are typically discarded after BM infusion. As defined by The International Society for Cellular Therapy Position Statement the MSCs were analyzed to verify the positivity to the markers CD90, CD73, CD105, and the negativity for CD45-34–14, CD19, and HLA-DR and for their capacity to differentiate in osteogenic, adipogenic, and chondrogenic cells after stimulation for three weeks using specific media (Miltenyi Biotec, Bergisch Gladbach, Germany).

MSCs were darkly exposed to 10 scalar dilutions of CuS NPs and CuS@C NPs, ranging from 100 μg/mL to 0.19 μg/mL, for 24 and 48 h. For both NPs type the concentration refers to μg/mL of CuS. During exposure, cells were observed under an optical microscope. At each time point (24 and 48 h), the media containing the NP were discarded and new media added to analyze the mitochondrial/metabolic activity and cell viability by the MTT (3-(4,5-dimethylthiazol-2-yl)-2,5-diphenyl-2H-tetrazolium bromide) assay. Cells were incubated with a 12 nM MTT stock solution at 37 °C for 4 h in the dark (Vybrant MTT Cell Proliferation Assay Kit V-13154, Molecular Probes Europe BV, ThermoFisher, Waltham, MA, USA). The water-insoluble formazan crystals formed during this process were solubilized by adding 50 μL of Dimethyl sulfoxide (DMSO). Samples were incubated at 37 °C for 10 min, and absorbance was measured at 560 nm using a GloMax Discover Microplate Reader (Promega, Madison, WI, USA). The optical density (OD) values obtained were used as a proxy for formazan concentration, directly proportional to the intracellular reduction of MTT. To account for baseline variability, untreated MSCs were used as the viability control, set to 100 %, while MSCs treated with Triton X-100 served as the mortality control, set to 0 %. Data normalization was performed using GraphPad Prism version 8.4. Statistical analysis was conducted to identify significant differences in cell viability among treatment conditions. A Friedman test was employed to compare overall group differences, followed by Dunn's multiple comparison test to determine specific pairwise differences between the viability control and each CuS NP treatment condition.

3. Results and discussion

3.1. Synthesis and tuning the optical properties of CuS NPs

For the synthesis, $Cu(NO_3)_2$ and Na_2S were chosen as inorganic precursors [55–57] in a 1:1 ratio, while PVP was used as capping agent and water as reaction medium. With the aim of tuning the optical properties of CuS NPs without altering their chemical composition, we maintained the constant concentration of inorganic precursors at 1 mM and varied the PVP concentration between 0 and 2 mM. The hot-injection technique was applied for delivering the S precursor,

which allowed effective reactant mixing and no provisional temperature drop and served as an effective technique for minimizing temporal overlapping of the nucleation and the growth stages, with the aim of producing NPs uniform in size and shape [32].

The crystalline phase of prepared NPs was investigated by X-ray diffraction (XRD) analysis. XRD pattern of CuS NPs synthesized using 0.2 mM of PVP is shown in Fig. 1A. The NPs display crystalline nature with well-defined peaks at 2θ = 27.69, 29.25, 31.80, 32.84, 47.97, 52.71, and 59.33° which are corresponding to the planes of (101), (102), (103), (006), (110), (108), and (116) of CuS hexagonal covellite structure respectively (JCPDS file no: 06–0564). The analysis also demonstrates the purity of prepared CuS NPs by showing a complete absence of any impurities and secondary phase due to other stoichiometries of copper sulfide. The average crystallite size of the nanoparticles was calculated using Scherrer's equation and found to be 13 ± 3 nm. The XRD pattern of CuS NPs prepared by using different concentrations of PVP (0.01, 0.2, 2 mM) similarly showed the typical peaks of covellite (Fig. SI–1) thus demonstrating that changing of PVP concentration did not affect the NPs crystal structure. The presence of the covellite phase was further confirmed by HRTEM (Fig. 1B), that allowed to identify particles with well-defined inter-planar spacing of 0.298 nm which corresponds to the *d* spacing for one of the planes (102) of hexagonal structured CuS crystal [57].

Fig. 1B depicts representative TEM images of CuS NPs prepared using the different concentrations of PVP. The NPs prepared without PVP and with the lowest PVP concentration tested (0.005 mM) exhibited an irregular morphology and aggregated NPs. Conversely, in the presence of higher concentration of PVP the NPs have defined isometric shape and narrow size distribution. Different particles morphologies were observed while changing the PVP concentration. At 0.01 mM PVP concentration, mainly spherical-like NPs were observed. While increasing the PVP concentration, along with spheres, larger hexagonal particles, the typical morphology of covellite crystals, appeared. Some particles with triangular shape were also formed at high PVP concentration, which might consist in irregular hexagonal particles. The size distribution of the particles prepared using different PVP concentrations were determined by analysis of TEM micrographs and reported in Fig. 1C. The results indicate an increase in mean size with PVP concentration. Moreover, the cumulative count analysis also shows a significant difference in the size distribution with 0.01 mM PVP - CuS NPs showing that almost 50 % of particles (X50) were less than 5.9 nm (±0.1) whereas for 2 mM PVP the 50 % was less than 7.5 nm (±0.1), confirming their trend.

The absorption spectra of CuS NPs prepared using different concentrations of PVP were measured by UV–vis–NIR spectroscopy, as shown in Fig. 1D. The strong absorption in the NIR range originates from the collective oscillation of valence-band free carriers (holes) on the surface of CuS NPs, resulting in the LSPR effect, while the absorption in the visible range is due to exciton transition [32,58,59]. Recorded spectra clearly elucidated that PVP concentration plays a significant role in determining both intensity and position of the plasmonic peak (λ_{max}). The particles prepared without PVP show a very low and broad LSPR profile, likely due to poor colloidal stability of the bare CuS NPs in water medium. In fact, the presence of large particles aggregates, as evidenced

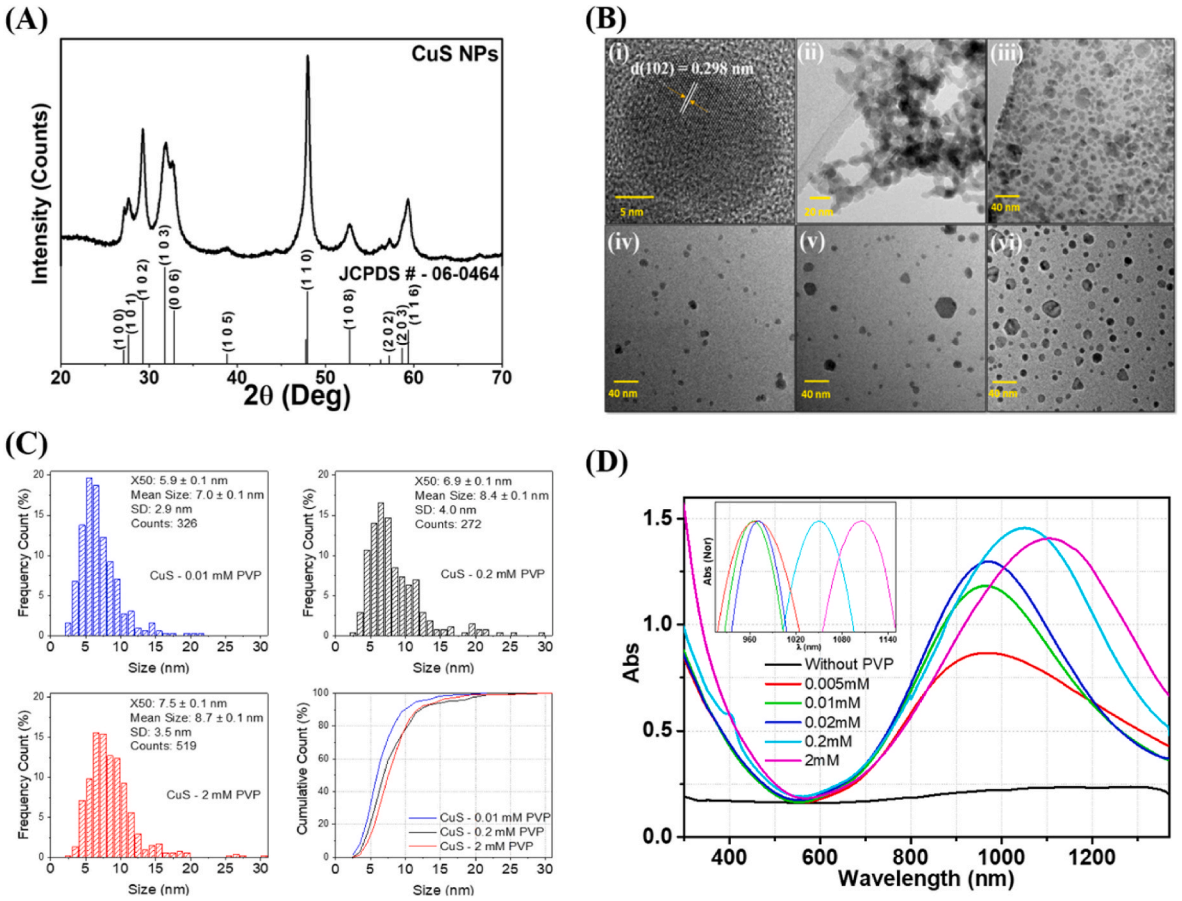

Fig. 1. Physico-chemical characterization of CuS nanoparticles synthetized with different PVP concentrations. (A) XRD pattern of 0.2 mM PVP-CuS NPs with standard JCPDS data. (B) (i) high resolution TEM image of 0.01 mM PVP-CuS NPs; TEM images of CuS NPs prepared using different concentration of PVP: (ii) without PVP (iii) 0.005 mM (iv) 0.01 mM (v) 0.2 mM (vi) 2 mM of PVP. (C) Size distribution histogram of CuS NPs prepared using different concentration of PVP and its cumulative count profile (D) UV–Vis–NIR absorbance spectra recorded on CuS NPs colloidal suspension (0.35 mM) prepared using different concentrations of PVP. Inset: normalized spectra of the samples.

from TEM analysis (Fig. 1B), lead to quick sedimentation as visually observed. When PVP concentration was increased from 0.005 mM to 0.2 mM the absorbance value increases gradually and the λ_{max} was red shifted whereas when the PVP concentration was further increased to 2 mM, a strong red shift was observed while the absorbance slightly decreased (Fig. 1D). Moreover, the width of the LSPR peak decreased when the PVP concentration increased from 0.005 mM to 0.02 mM and again increased for higher PVP concentrations. As evidence from TEM analysis the particles prepared without PVP and 0.005 mM PVP were bigger in size and tended to aggregate. Since the peak width is related to particles monodispersity [60,61] and likely to particles aggregation state [62,63], the particles prepared at these conditions have broad and asymmetric LSPR profile. At the intermediate PVP concentration (0.01 or 0.02 mM) the particles were more monodispersed hence shows the narrow and symmetric LSPR profile. When the PVP concentration was further increased, particles started to lose their monodispersity, but not colloidal stability, leading to slightly broader but symmetric LSPR profile. Moreover, the band gap value of the prepared CuS NPs calculated from the absorption spectra using Tauc plot (Fig. SI–5) showed that as the PVP concentration increased the band gap value slightly decreased from 2.40 eV for 0.01 mM to 2.28 eV for 2 mM PVP synthesized CuS NPs. These band gap values are within the range of values of previously reported covellite CuS nanostructured materials [32,59,64].

The increase of particle size can explain the differences observed in the LSPR maxima. It is already well-established that the red-shift in the NIR absorption band is due to the decrease in free carrier density in the covellite nanocrystals [30] that in turn depends on the particles size [32]. In the present case the free hole carrier density of each sample calculated by using Drude model [28,30] was found to be approximately equal to 5.0×10^{21}, 4.1×10^{21} and 3.7×10^{21} free carrier/cm^3 for 0.01, 0.2 and 2 mM PVP-CuS NPs, respectively. However, we cannot exclude a partial effect due to a possible increase of PVP coating thickness on CuS NPs when the PVP concentration was increased, which would lead to an increase of the dielectric environment in the surrounding of the NPs and consequently red-shifts the LSPR maximum [65].

The LSPR spectra of CuS batches prepared by independent synthesis (Fig. SI–6) were almost overlapped demonstrating the high reproducibility of the proposed method. The kinetic of formation of CuS NPs during the synthesis can be empirically measured by the time of change of the brown color that appears after the injection of the sulfide ions precursor into the typical green of covellite NPs. The appearance of the green color was almost immediately when the NPs were prepared without PVP while increasing PVP concentration the time proportionally increased. A comparison of the kinetics of formation at PVP concentration of 0.01 and 2 mM evaluated by UV–vis–NIR spectrophotometry is reported as supplementary materials (Fig. SI–7).

PVP is used in the synthesis of transition metal chalcogenides since it acts as a capping agent, efficiently providing colloidal stability to the NPs [66]. Our data clearly demonstrate that PVP does not act only as stabilizer and capping agent, but it also plays a role in tailoring the particles size during the synthesis of CuS NPs, an effect that was reported previously for other nanomaterials like copper oxides [67,68] and zinc sulfide [69]. The fact that the kinetics of formation of NPs was slowed down as PVP concentration increased is a clear indication that the size growth is not driven by a confinement effect and that PVP kinetically control the crystal growth.

One possible explanation of the role of PVP may derive from the known ability of the polymer to act as a ligand for several metal ions including copper due to the presence of amide groups [70,71]. Therefore, PVP might act as reservoir of Cu^{2+} ions, kinetically controlling the ions availability. In the absence or at low concentration of PVP the high concentration of free Cu^{2+} ions induces the fast nucleation of a high number of NPs, while at high PVP concentration the number of nuclei formed is low since Cu^{2+} ions are not all available. During time, Cu^{2+} ions bound to PVP are released forming new layers on pre-formed nuclei, leading to the growth of particles. It is already well established that when inorganic particles nuclei are present, the system tends to evolve by growing up the already formed particles instead of forming new nuclei, especially when the precursor concentrations are low [72]. Moreover, similar kinds of behavior have been reported earlier for ZnS nanocrystal synthesized using PVP [69].

Overall, these results demonstrate that CuS NPs size and shape, and consequently plasmonic properties, can be modulated by PVP concentration without affecting the crystal structure.

3.2. Chemical stability of CuS NPs in aqueous media

As discussed in the introduction CuS NPs are poorly stable in aqueous media, thus limiting post-synthesis treatments. Albeit there is clear evidence that CuS NPs stability is highly sensitive to temperature and pH of the solution [73] a systematic investigation of their stability in wide range of pH is not available. With the aim of overcoming the CuS instability we investigate the effect of temperature and pH on the chemical stability of prepared CuS NPs, choosing 0.2 mM PVP-CuS NPs as model sample. The NPs were incubated in different conditions, and the degradation monitored by measuring changes of the amplitude of the plasmonic peak over time and by quantifying the release of Cu^{2+} ions using BCA test. The results are shown in Fig. 2.

CuS NPs were degraded in all the conditions tested but as expected, the degradation extent and the time was dependent by temperature and pH. In fact, while no variation in the absorbance and negligible amount of copper released was observed at 4 °C, a large variation in absorbance and a substantial release of copper ions was observed when the sample was stored at physiological temperature (37 °C). At this temperature, the degradation was rapid, and almost 60 % degradation occurred in 7 days of exposure (Fig. 2A). These results agree with data previously reported [73]. The effect of pH on the stability of CuS NPs is reported in Fig. 2B. As inferred by the absorbance of the plasmonic peak, particles incubated at extreme acidic and basic conditions were degraded at faster rate compared to intermediate pH conditions. A significant amount of degradation occurred already at 4 h of incubation time which highlighted that particles had very poor stability at these extreme pH conditions. The loss of plasmonic absorbance of the CuS NPs incubated at different pH conditions over a period almost parallel with the Cu^{2+} ions release. Unexpectedly, CuS NPs incubated in phosphate saline buffer (PBS) at pH 7.4, and pH 11 (NaOH) showed low amount of Cu^{2+} ions released, likely because of the formation of insoluble species. In fact, we noticed the formation of a light-blue precipitate after 7 days of incubation at pH 7.4 in PBS and a black precipitate in the case of incubation at pH 11. The ATR-FTIR analysis of the precipitates (Fig. 2C) revealed the formation of copper phosphate in PBS, as inferred by the strong peaks at 1044 and 1135 cm^{-1} attributed to P–O and P═O vibrations of phosphate group and the presence of two bands at 559 and 623 cm^{-1} attributed to the bending vibrations of bridging phosphorous such as O═P–O [74,75]. The precipitate formed at pH 11 was identified as Cu$(OH)_2$ or mixture of CuO/Cu$(OH)_2$ by the presence of intense peaks around 1646 cm^{-1} and 1124 cm^{-1} are ascribed to –OH bending vibrations combined with Cu atoms. The peaks at 610 and 501 cm^{-1} are associated with stretching vibration of the Cu–O bonds in CuO and Cu$(OH)_2$ [75]. Moreover, the strong peak at 3348 cm^{-1} due to the stretching mode of the hydroxyl groups.

The results indicate that the dissolution of CuS particles is the major mechanism leading to the loss of the plasmonic properties.

3.3. Synthesis of CuS@C core-shell NPs

As discussed in the introduction, the application of a shell is a common strategy to control the degradation of NPs. In the present case amorphous carbon was identified as possible material for the shell. Among the different synthetic approaches to produce carbon nanoparticles, the hydrothermal carbonization (HTC) of biomasses is the most simple and effective water-based method [76]. Using HTC method,

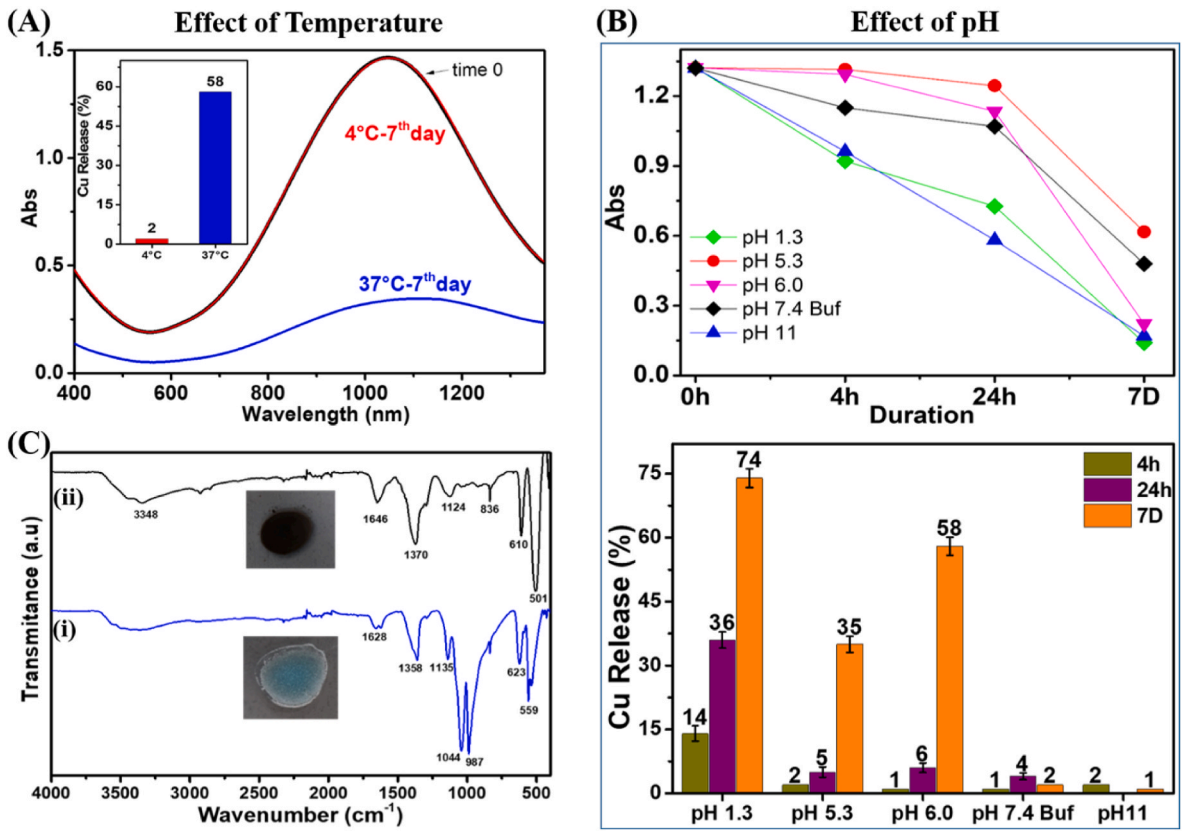

Fig. 2. Chemical Stability of 0.2 mM PVP-CuS NPs in different conditions. (A) UV–vis–NIR absorption spectra of CuS NPs suspension incubated at 4 °C or 37 °C for 7 days (pH 6.0). Inset: Amount of copper released evaluated by BCA test and expressed as % by respect to the initial concentration (B) Top panel: Absorbance value of plasmonic peak at different time points measured on the CuS NPs suspensions incubated at different pH (37 °C); pH 7.4 was obtained by using PBS (10 mM); Bottom panel: Amount of copper released evaluated by BCA test and expressed as % by respect to the initial concentration (C) ATR-FTIR spectra of precipitated powder formed by incubation of CuS NPs in (i) PBS solution and (ii) NaOH solution. Inset: images of the dried precipitated powders.

we previously synthesized carbon nanoparticles with high colloidal stability and good biocompatibility using glucose as a precursor [77,78]. A similar synthetic methodology was adapted here to generate a carbon shell on CuS NPs. The hydrothermal process was previously used by Zhang et al. to synthetize CuS@C core-shell nanoparticles [46]. However, in that case, the plasmonic peak related to CuS NPs was lost during the synthesis. Based on our results, this was likely due to the instability of CuS NPs at high temperatures which is necessary for carbon shell formation. As strengthen our prediction, the CuS NPs treated by hydrothermal heating at 190 °C for 3 h showed a complete loss of plasmonic peak (Fig. 3A).

The mechanism of covellite NPs degradation in aqueous environment is complex and involves oxidative reactions. Since the first step of this process is the dissolution equilibrium of CuS into Cu^{+}, S^{2-} and S_2^{-} ions [79], we hypothesized that it could be inhibited by supplying additional copper or sulfur ions to the system. We therefore tested the stability of CuS NPs at 190 °C for 3h in the presence of 2 mM of $Cu(NO_3)_2$ or 2 mM of Na_2S. In the first case the absorbance spectra of the suspension after the reaction showed a small plasmonic peak, suggesting that only some plasmonic NPs remained (Fig. 3B). More efficacious was the addition of Na_2S as inferred by the presence of the peak at 1015 nm (Fig. 3C). However, when the concentration of Na_2S increased to 10 mM to further shift the dissolution equilibrium, we unexpectedly observed a substantial suppression of the plasmonic peak (Fig. 3C). This can be explained by the strong basic environment induced by the high concentration of Na_2S, as our previous test demonstrated the very poor stability of CuS NPs in basic pH condition (Fig. 2B). To avoid this effect, we selected L-cysteine as sulfur source. This molecule, previously used as sulfur source under hydrothermal condition for the synthesis of CuS NPs, was an ideal candidate as stabilizer since it is an amphoteric and non-toxic substance [80]. As shown in Fig. 3D we successfully prevented the CuS NPs dissolution by increasing the L-cysteine concentration up to 3.8 mM. To the best of our knowledge this is the first time that an S-source was used to increase the stability of CuS NPs at high temperatures.

With the above understanding of the CuS NPs behavior under the hydrothermal treatment we repeated the reaction in the presence of glucose as carbon precursor. In this case, when the highest concentration of cysteine was used, a mud-like product was likely obtained due to the aggregation of the particles. By lowering the L-cysteine concentration to 1 mM, we successfully obtained CuS@C NPs with good NIR absorbance (Fig. 4A). We also observed a red-shift in the LSPR λ_{max} of the CuS@C NPs to 1118 nm, an effect likely due to the change of refractive index at the particle surface induced by the carbon shell [65]. The width of the plasmonic peak slightly increased after the treatment, an effect that can be due to a partial aggregation of the particles. To increase their monodispersity, a small amount of PVP (0.01 mM) was added into the solution before the hydrothermal treatment. In this case the peak became narrower, and the intensity increased together with a blue shift ($\lambda_{max=}$1072 nm), demonstrating the efficacy of the PVP addition.

The XRD pattern of the optimized product (Fig. 4B) clearly indicated that the CuS@C NPs retained their CuS covellite structure. Moreover, the CuS@C NPs sample showed more intense and resolved XRD peaks compared to the precursor CuS NPs, which might be due to an increase of crystallites size. TEM analysis of the optimized CuS@C (Fig. 4C) revealed that the amorphous carbon was perfectly coated on the surface of CuS NPs. All the particles were encapsulated into a carbon shell with thickness of 6.1 ± 1.3 nm. The mean size and the standard deviation of

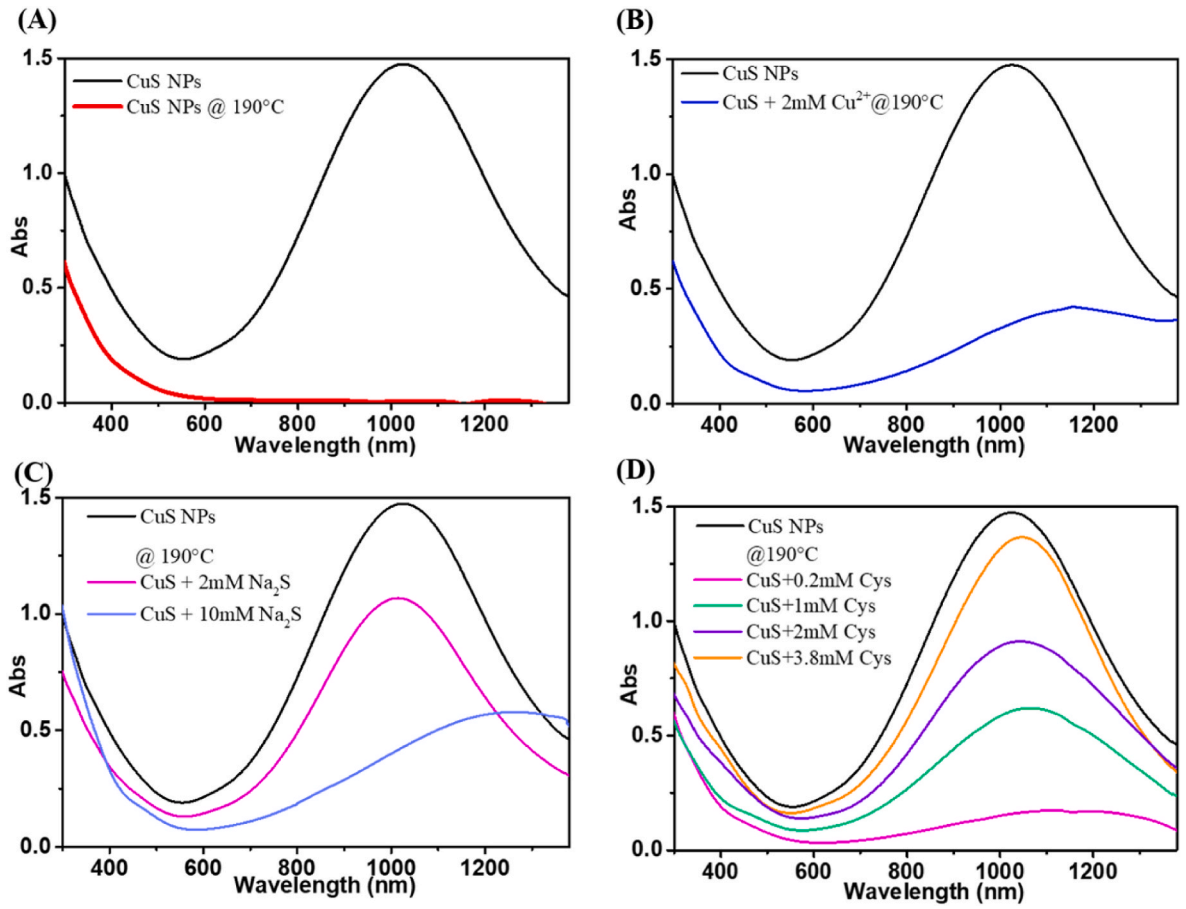

Fig. 3. Stability of CuS NPs during hydrothermal treatment. UV–vis–NIR absorbance spectra of 0.7 mM CuS NPs (0.2 mM PVP-CuS) under hydrothermal treatment at 190 °C for 3 h in various conditions (A) without any addition (B) with 2 mM of $Cu(NO_3)_2$ (C) with different concentration of Na_2S and (D) with different concentration of L-Cysteine (spectra were recorded using CuS colloidal solution diluted by water in 1:1 ratio).

the distribution of CuS@C NPs was found to be 25.9 ± 10.9 nm with the CuS core of 14.4 ± 10.0 nm (Fig. 4C inset). These results highlight that during the coating process the size of CuS NP slightly increased, likely following a partial precursor-particles dissolution and re-formation, an Ostwald ripening-like process. The ζ potential measured at similar pH and conductivity by ELS (Fig. 4D) was shifted from the neutral value of the PVP coated CuS NPs (−1.4 ± 0.5 mV) to a value of −24.6 ± 1.1 mV, suggesting the presence of a negative charge at the surface. The negative charge likely derives by the dissociation of carboxylic groups, since these functionalities are typical of carbon nanoparticles produced by the hydrothermal method [81]. The mean hydrodynamic diameter of the CuS@C NPs in water measured by dynamic light scattering was found to be 43 ± 14 nm (Fig. SI–9A), compatible with the mean geometrical diameter measured by TEM. Since DLS is known to overestimate large particles due to their higher intensity of the scattered light, the value indicates the absence of large particles or aggregates [82]. The LSPR spectra and DLS measurements of four CuS@C batches prepared by independent synthesis (Figure SI-9B, C) were almost overlapped demonstrating the high reproducibility of the proposed method. As expected from our previous study [81], increasing the amount of glucose to 20 mg/mL leads to an increase of the carbon shell thickness to 16.9 ± 2.4 nm. However, particles were found to aggregate as inferred by TEM analysis (Fig. SI–10). Note that a one-pot synthesis methodology by putting all the precursor together in the autoclave ends up with plasmonically inactive materials, indicating that precursor CuS NPs are needed in the developed procedure.

3.4. Photothermal property of CuS and CuS@C NPs

The strong LSPR absorption of as-synthesized CuS and CuS@C NPs in the NIR region motivates us to investigate their potential in photothermal conversion using a 915 nm laser. The temperature changes of the aqueous dispersion containing CuS or CuS@C NPs under the irradiation of 915 nm laser with a power density of 650 mW/cm^2 were recorded as a function of time under continuous irradiation until steady state temperature was reached, as shown in Fig. 5A. The concentrations were adjusted to have the same amount of CuS (100 μg/mL). The temperature of the aqueous dispersion containing CuS NPs rapidly increased, reaching 43.5 °C in 5 min (ΔT = 6.5 °C) and attained the highest temperature of 45.1 °C (ΔT = 8.1 °C) under continues irradiation for 15 min. CuS@C NPs appeared even more efficient, reaching 44.1 °C in 5 min (ΔT = 7.1 °C) and attaining the highest temperature of 46.0 °C (ΔT = 8.95 °C) under continues irradiation for 15 min. This temperature elevation, achieved by irradiation with conservative and safe low power density, is more than sufficient to induce the hyperthermia and cell death. Note that when pure water was irradiated, an increase of 1.2 °C was observed. The photothermal conversion efficiency (PCE) of CuS and CuS@C NPs were calculated using the method reported by Zhang et al. [51] (for detail calculation, see the experimental section and SI). The PCE of the CuS was found to be 50 %, noticeably higher than previously reported for CuS NPs like Pillararene-Capped CuS (34 %) [83] and cysteine capped CuS NPs (38 %) [84]. This high efficiency could be ascribed to high NIR absorbance and low light scattering, as a consequence of the high monodispersity, small size and absence of aggregation of prepared CuS NPs. However, the measured

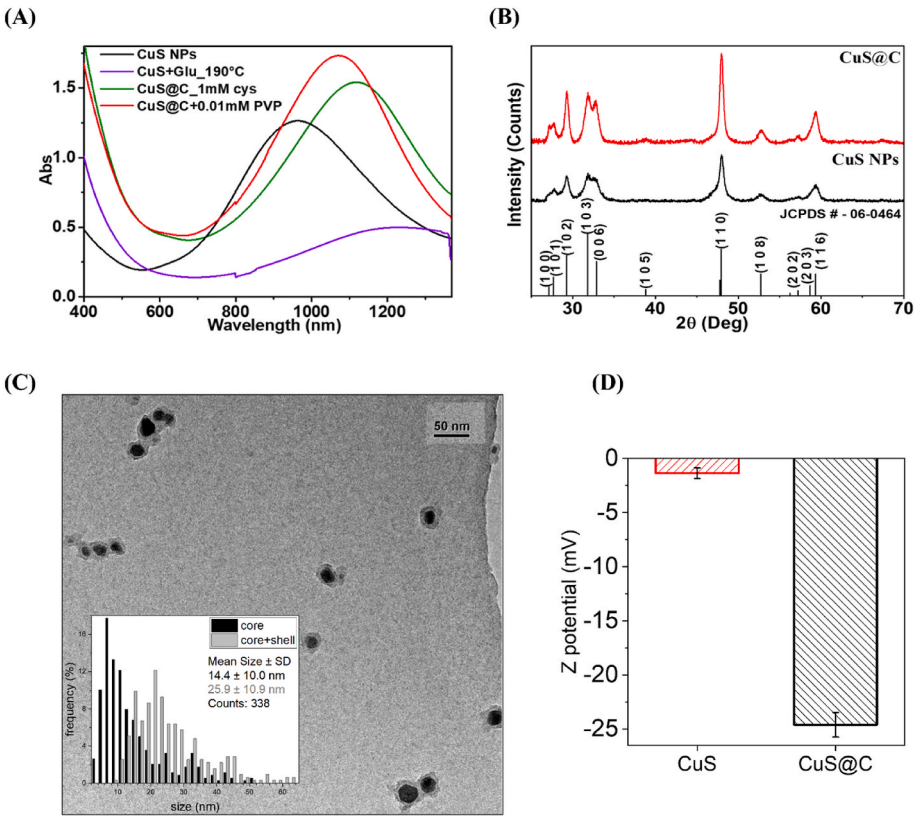

Fig. 4. Physicochemical properties of CuS@C NPs. (A) UV–vis–NIR absorbance spectra of CuS NPs (0.7 mM) after hydrothermal treatment in different conditions compared with pristine CuS NPs (black line): 5 mg/mL of glucose (violet); 5 mg/mL of glucose and 1 mM of L-Cysteine (green); 5 mg/mL of glucose, 1 mM of L-cysteine and 0.01 mM of PVP (red) (all spectra were recorded using NPs colloidal solution diluted by water in 1:1 ratio). (B) XRD pattern of CuS@C NPs compared with 0.01 mM PVP-CuS NPs (C) TEM images of CuS@C NPs; Inset: Size distribution histogram of the CuS cores (black) and CuS@C particles (grey); SD: standard deviation related to the width of the distribution; counts: number of particles measured on the TEM images. (D) ζ potential values measured for of 0.01 mM PVP-CuS NPs and CuS@C NPs.

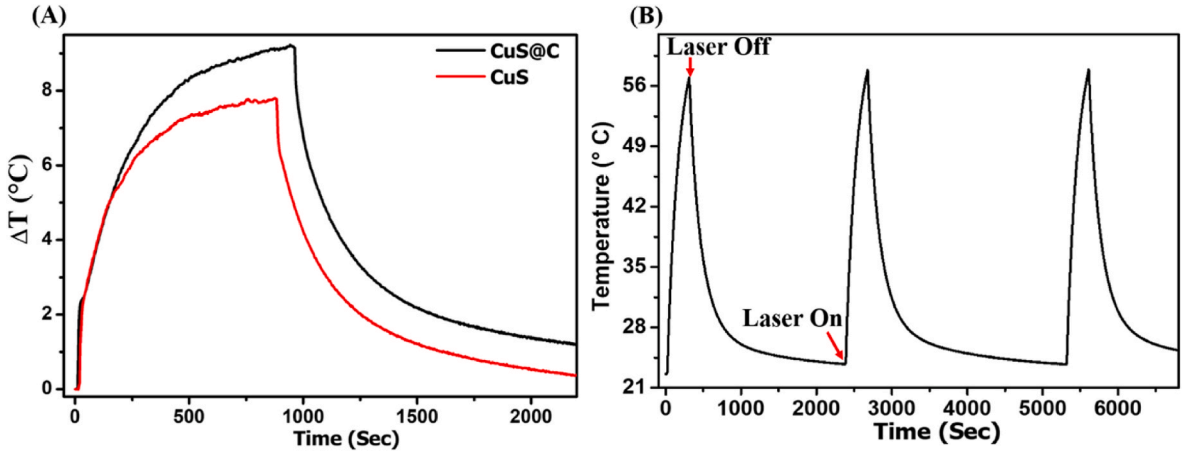

Fig. 5. Photothermal property of CuS and CuS@C NPs: (A) Temperature profile up to 2200 s of CuS and CuS@C NPs aqueous suspensions (CuS 100 μg/mL) irradiated by 915 nm laser light with power of 650 mW/cm^2. Irradiation was performed until steady state temperature followed by natural cooling with laser light turned off (B) Photothermal stability test of CuS@C NPs with laser power 2360 mW/cm^2.

PCE values of 50 % is in line with that recently reported for PVP capped CuS NPs (51 %) [43] or chitosan functionalized CuS NPs (47 %) [85].

The PCE value for CuS@C NPs was found to be 52 %, much higher than reported for CuS NPs coated with inorganic material such as mesoporous silica (29.5 %) [86], or silica (31.2 %) [87]. The higher PCE value of the prepared CuS@C NPs may be due to their narrower NIR absorption spectra compared to those of the above mentioned silica-coated CuS NPs, ascribable to a less agglomerated and more monodisperse nature of the CuS core and the composite presented here.

The observed slightly higher PCE of CuS@C by respect to its CuS precursor could be attributed to a possible contribution of the carbon shell to photoconversion [81]. Note that CuS@C are predicted to have even more efficiency when a laser in the II therapeutic window would be used as its λ_{max} has red shifted to 1074 nm [88,89].

Another important property needed for PTA applicability is photothermal stability, to ensure that they can maintain their PCE under high intensity illumination. Photothermal stability is particularly relevant for molecular PTA, or for inorganic PTA coated with organic compounds. For example, the applicability of the FDA-approved organic PTA compound indocyanine green is known to be limited by rapid photodegradation [90]. However, also some nanostructured inorganic PTA like Au nanorods, which have excellent photothermal conversion efficiency, can present photostability problems after prolonged exposure to laser light [91]. The photothermal stability of the CuS@C NPs was tested using the 915 nm NIR laser at high power irradiation (2360 mW/cm^2) for 5 min (laser on) and followed by naturally cooling down to room temperature without laser irradiation (laser off) for three cycles (Fig. 5B). The particles exhibited robust performance even after

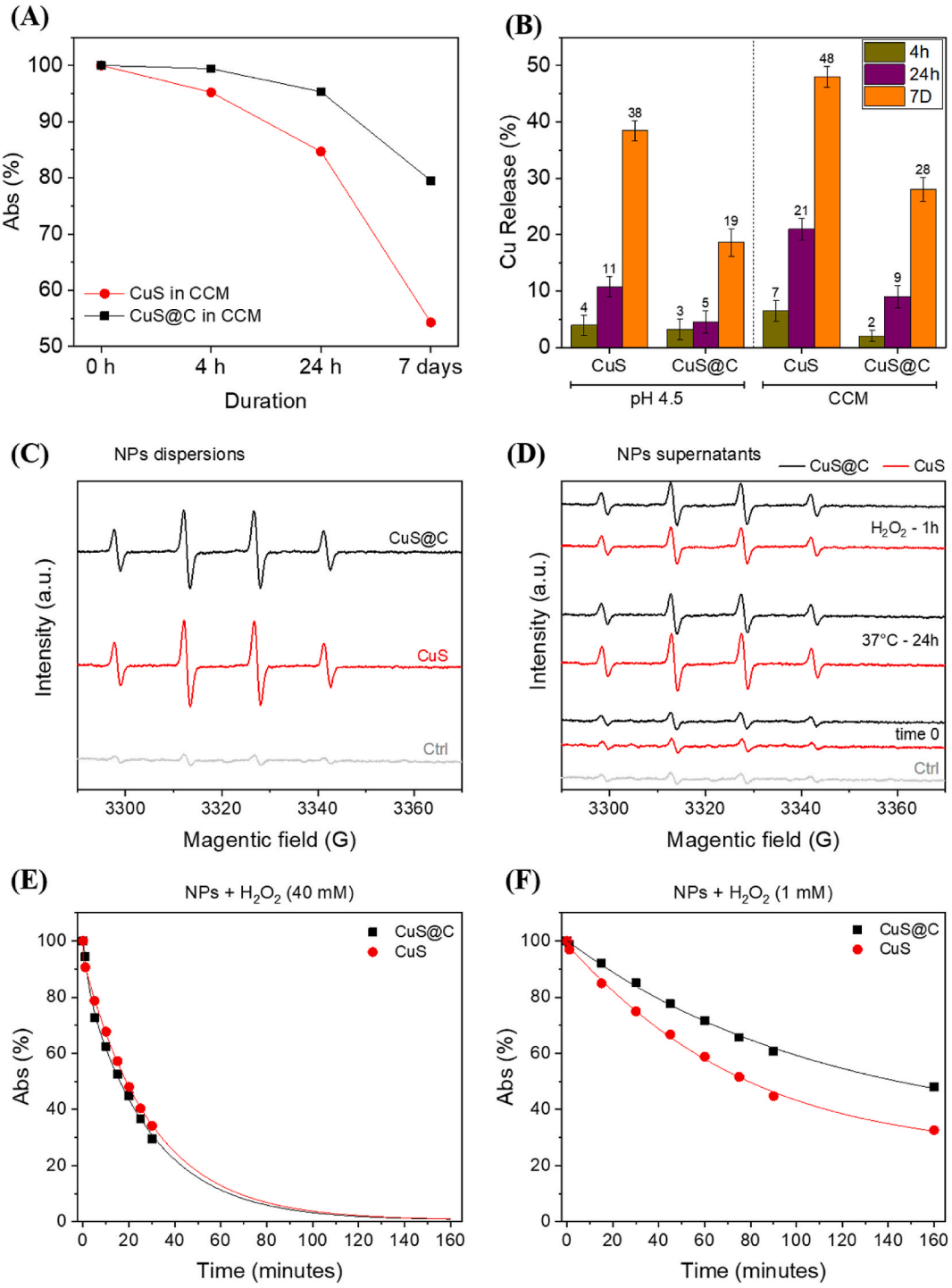

Fig. 6. Reactivity and stability of CuS and CuS@C in simulated physio-pathological conditions: (A) Variation of NIR absorption of CuS and CuS@C NPs incubated in cell culture media at 37 °C; (B) copper ions released by CuS NPs and CuS@C NPs incubated at pH 4.5 and in cell culture media at 37 °C; (C) Hydroxyl radical generation by CuS and CuS@C NPs in the presence of 40 mM H_2O_2 and 177 mM DMPO in PBS 10 mM, pH 7.4; (D) Hydroxyl radical generation by Cu^{2+} ions released by CuS and CuS@C NPs incubated at 37 °C for 24h or at room temperature for 1h in presence of 40 mM H_2O_2. Variation of NIR absorption of CuS and CuS@C NPs in presence of (E) 40 mM and (F) 1 mM H_2O_2 over time. Experimental data were fitted with two-phase exponential decay function. R^2: CuS 40 mM - 0.9999; CuS@C 40 mM - 0.9986; CuS 1 mM - 0.9982; CuS@C 1 mM - 0.9980).

undergoing three cycles of heating reaching 56 °C, affirming their superior performance as PTT agent.

3.5. Effect of the carbon shell on stability and reactivity of CuS in simulated physio-pathological conditions

The effective capacity of the carbon shell to control the stability and the biological reactivity of the CuS core was evaluated at 37 °C in solutions simulating the physiological fluids. Cell culture media (CCM) with the addition of Foetal Bovine Serum (FBS) was used as solution similar to plasma, and phosphate buffer (PB) at pH 4.5 to simulate the pH found in lysosomes of healthy cells and in the tumor microenvironment.

CuS and CuS@C NPs were incubated in the CCM or in PB at pH 4.5 up to 7 days and the variation of the plasmonic peak and the release of Cu^{2+} ions during time measured (Fig. 6 A&B). For both samples the extent of Cu^{2+} ions released had a trend similar to the loss of LSPR absorption of NPs. However, the process was significantly reduced by the carbon shell. CuS NPs incubated in CCM released 21 % of Cu^{2+} ions in 24 h and 48 % in 7 days, while CuS@C released only the 9 % and 28 %, respectively. Similarly, at pH 4.5 the copper ions released by CuS NPs was 11 % in 24 h and 38 % in 7 days while in the case of CuS@C NPs it was 5 % and 19 %, respectively. The results prove the ability of carbon shell to control the copper ions release without completely inhibit the dissolution of NPs, likely because of some porosity of the carbon shell.

The colloidal suspensions of CuS@C NPs stored at 4 °C shows a very good stability up to 1 week. After that it slowly starts degrading losing around 4 % after 2 weeks and 12 % after 4 weeks, as inferred by vis-NIR spectra (Fig. SI–13).

Hydrogen peroxide is a long living ROS naturally produced by the enzyme superoxide dismutase (SOD) in cells. Its concentration is low in healthy cells, but high in the lysosomes of phagocytic cells, the most important components of the innate immune system [92], and in tumor microenvironment [93]. CuS NPs are well known Fenton-like catalysts [94]. In the presence of hydrogen peroxide they generate hydroxyl radicals by following Cu^{+}/Cu^{2+} redox cycling. The generation of ROS and the release of copper ions make CuS NPs a bio-reactive material, able to interfere with the redox homeostasis of cells. When produced in high amount, these species can induce cell death by different pathways included immunogenic cell death [40]. Note that copper-based NPs were shown to be able to reduce the immune response [95,96].

The Fenton-like reactivity of CuS and CuS@C NPs was studied by EPR spectroscopy. The EPR spectra recorded for CuS and CuS@C in the presence of hydrogen peroxide and the spin trap DMPO are shown in Fig. 6C. For both materials the typical signal of the DMPO/$OH^{\cdot}$ adduct was observed (intensity 1:2:2:1, $a^N = a^H = 14.5$ G) with no significant difference between the two materials. This suggests that the shell does not inhibit the reaction of H_2O_2 with the surface, or with free copper ions. In fact, as already observed in Fig. 6A and B, the carbon shell slows down but does not completely inhibit the dissolution of CuS. To investigate the role of free ions, the Fenton-like activity has been measured on the supernatant of freshly purified CuS and CuS@C NPs, and after their incubation at 37 °C for 24h (Fig. 6D). While the first supernatant was not reactive, after 24 h of incubation at physiological temperature an intense signal was observed with the supernatant of both materials, in agreement with the kinetics of release of the ions (Fig. 6B). To investigate the role of H_2O_2 in the dissolution of CuS NPs, we also investigate the generation of hydroxyl radical from H_2O_2 on the supernatant obtained following incubation of the NPs for 1 h with H_2O_2 at the concentration used in the EPR experiments (40 mM). In this case, a signal was observed for both materials, indicating that H_2O_2 increases the reactivity of both materials promoting the release of copper ions. To confirm this, the plasmonic band of CuS and CuS@C NPs in the presence of different concentrations of hydrogen peroxide was measured (Fig. 6E and F). The data clearly show that hydrogen peroxide largely affects the stability of both materials, in a concentration-dependent way. In fact, while at very high concentration (40 mM) CuS and CuS@C were almost totally degraded after 30 min at a similar extent, at concentration closer to that found in cells (1 mM), CuS@C NPs appear more stable than CuS NPs. This suggests that the carbon shell might contain the reactivity in healthy cells leaving unaltered the cytotoxic potential in tumors. To confirm that hydroxyl radicals generated by CuS and CuS@C NPs were due to a Fenton-like reaction, the EPR spectra were also recorded in the absence of H_2O_2 (Fig. SI–15). In this case no signal was observed.

3.6. Effect of the carbon shell on the cytotoxicity toward mesenchymal stem cells

MSCs are multipotent stromal cells capable of differentiating into various cell types and are widely used in biomedical research, including drug delivery, tissue engineering, and in the development of novel therapeutic approaches [97–100]. MSCs are a suitable model for acute drug toxicity screening of substances [101]. They are human primary cell cultures that exhibit a longer in vitro propagation by respect to other primary cells making them a more reliable model compared to immortalized or transformed cell lines. Here, CuS NPs and CuS@C NPs have been tested for their effect on MSCs viability as preliminary test to assess their cytotoxicity.

The analysis of cell metabolic activity and related viability after 24 h and 48 h of exposure to various concentrations of CuS NPs (left panels) and CuS@C NPs (right panels) is reported in Fig. 7. After 24-h exposure, no significant differences in cell viability were observed at any concentration of CuS or CuS@C compared to the viability control. This indicated that short-term exposure to both NPs formulations did not significantly alter mitochondrial/metabolic activity at the tested concentrations. Conversely, after 48 h of exposure significant differences emerged depending on the NPs type and concentration. At low concentrations of CuS NPs (0.23–0.46 μg/mL), no significant changes in viability were observed compared to the control. At intermediate concentrations (from 0.8 μg/mL to 6.25 μg/mL), a significant increase in metabolic activity was observed, as indicated by one, two, or three asterisks denoting statistical significance ($p < 0.05$). This effect suggests a potential stimulatory effect of CuS NPs at these concentrations. At high concentrations (50, 100 μg/mL), a marked reduction in metabolic activity was detected ($p < 0.01$ and $p < 0.001$), likely associated with cytotoxicity and cell death, as also supported by optical microscopy images showing signs of cellular damage (Fig. SI–16).

In the case of CuS@C NPs (0.23–1.6 μg/mL), the metabolic activity remains fundamentally unaltered. At intermediate concentrations (3.1–12.5 μg/mL), a reduction in metabolic activity was observed ($p < 0.05$), correlating with cytotoxicity evident from optical microscopy images, which showed morphological signs of cell damage (Fig. SI–16). At high concentrations (25–100 μg/mL), a pronounced cytotoxic effect was observed ($p < 0.01$ and $p < 0.001$), consistent with decreased metabolic activity and visible cell death observed at the microscope.

These findings suggest a differential, time-dependent, and concentration-dependent response of MSCs to CuS and CuS@C NPs. While neither NP formulations affect viability after 24 h, significant effects were observed after prolonged exposure. Moreover, while CuS NPs induced an increased metabolic activity at intermediate concentrations and cytotoxic effects at the highest concentrations, CuS@C NPs exhibited a reduction in metabolic activity at intermediate concentrations and stronger cytotoxicity at high doses. The pro-proliferative effect of CuS at low doses agrees with a previous study on MSCs showing a similar trend for copper ions [102]. Copper ions are known to be involved in cell proliferation, respiration and redox homeostasis being a cofactor for various copper-dependent enzymes [103,104]. The absence of a pro-proliferative effect for CuS@C is likely due to the lower rate of dissolution of the CuS core. At high doses both NPs induce significant cytotoxicity, likely due to NPs uptake, and consequent intracellular release of copper ions, which are known to induce cell death by a peculiar mechanism called cuproptosis that follows intracellular copper

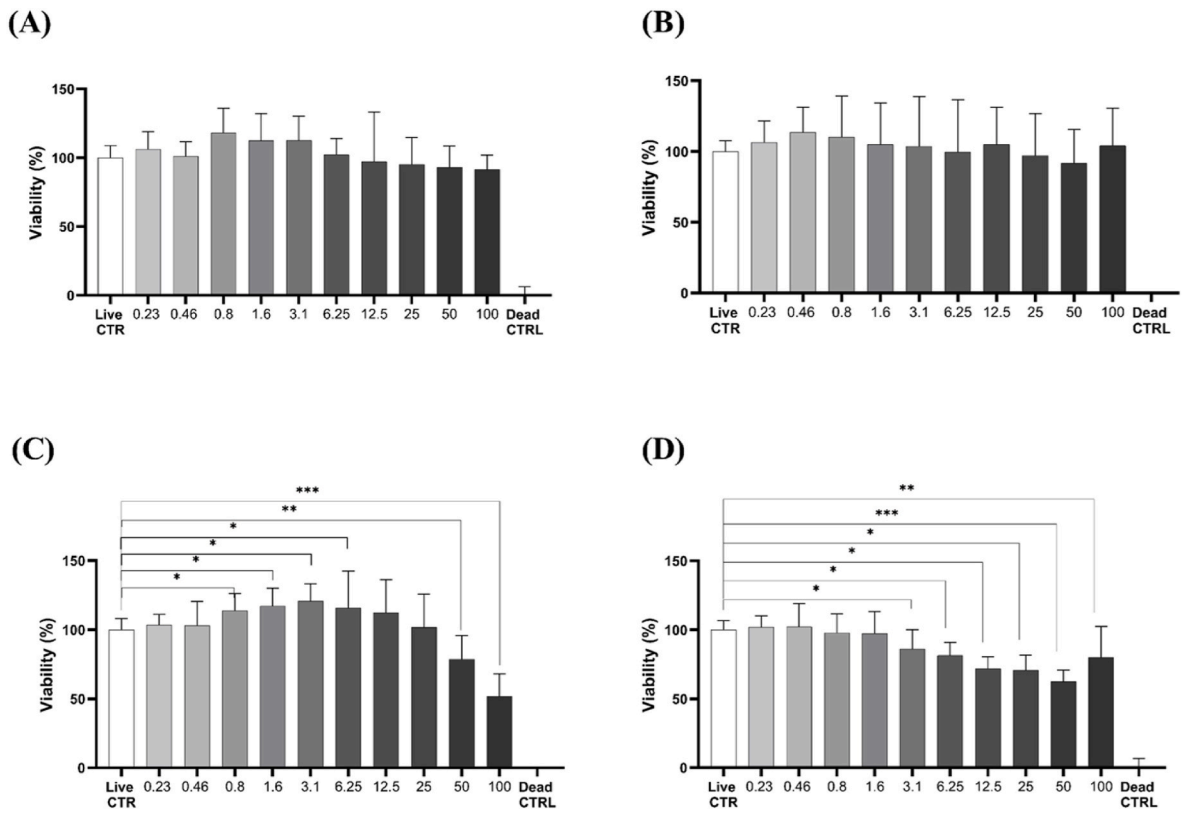

Fig. 7. Cell Viability Analysis of MSCs Exposed to CuS and CuS@C Nanoparticles for 24 and 48 Hours: The figure illustrates the effects of CuS NPs (left panels) and CuS@C NPs (right panels) on the viability of MSCs after 24 h (A, B) and 48 h (C, D) of exposure at concentrations ranging from 0.23 μg/mL to 100 μg/mL representing the means with standard deviations from three independent experiments. After 24 h of exposure to various concentrations of CuS NPs (A) and CuS@C NPs (B), respectively, no significant differences in cell viability are observed between the tested different concentrations and the viability control condition. In contrast, the bottom panels (48-h analysis) reveal significant differences in cell viability between specific concentrations of CuS NPs (C) and CuS@C NPs (D) compared to the viability control. These differences are indicated by statistical significance symbols (*, **, ***), corresponding to $p < 0.05$, $p < 0.01$, and $p < 0.001$, respectively. "Live Ctrl" represents the viability control, where untreated cells are set at 100 % viability in the normalization process. "Dead Ctrl" represents the mortality control, where cells were treated with Triton X-100 and set at 0 % viability. The viability of MSCs exposed to CuS and CuS@C NPs at different concentrations is expressed as a percentage relative to the Live Ctrl."

accumulation [103,104].

4. Conclusion

The novel synthetic approach herein presented allowed to synthesize colloidal CuS@C core-shell NPs with enhanced and narrow LSPR profile, high heat conversion efficiency of NIR light and superior photostability by using water as solvent. The carbon shell significantly improved the stability of CuS NPs in simulated biological conditions, and inhibited the proliferative effect of CuS, keeping unaltered the cytotoxic potential, thus increasing the potential of covellite as agent for systemic administration in solid tumors therapy. Further in vitro and in vivo studies will be necessary to validate the efficacy and the safety of CuS@C NPs following activation with NIR light.

CRediT authorship contribution statement

Sathish Shanmugam: Writing – review & editing, Writing – original draft, Validation, Methodology, Investigation, Formal analysis, Data curation, Conceptualization. **Francesco Barbero:** Writing – review & editing, Writing – original draft, Visualization, Validation, Methodology, Investigation, Formal analysis, Data curation, Conceptualization. **Aurora Bellone:** Validation, Investigation. **Alessia Giovanna Santa Banche Niclot:** Validation, Investigation. **Simone Miatto:** Validation, Investigation. **Guido Perrone:** Writing – review & editing, Resources. **Katia Mareschi:** Writing – review & editing, Visualization, Validation, Resources, Formal analysis. **Ivana Fenoglio:** Writing – review & editing, Supervision, Funding acquisition, Conceptualization.

Data availability

The authors state that all data supporting the results of this study can be found within the paper and its supplementary materials. If raw data in different formats are required, they can be provided by the corresponding author upon reasonable request.

Declaration of competing interest

The authors declare that they have no known competing financial interests or personal relationships that could have appeared to influence the work reported in this paper.

Acknowledgements

We acknowledge financial support from the ReUNITA project (Grant Agreement No. 101035810). The authors acknowledge the use of instrumentation as well as the technical advice provided by the National Facility ELECMI ICTS, node "Labo ratorio de Microscopias Avanzadas (LMA)" at "Universidad de Zaragoza".

Appendix A. Supplementary data

Supplementary data to this article can be found online at https://doi.org/10.1016/j.mtchem.2025.102765.

Data availability

Data will be made available on request.

References

[1] J.N. Anker, W.P. Hall, O. Lyandres, N.C. Shah, J. Zhao, R.P. Van Duyne, Biosensing with plasmonic nanosensors, Nat. Mater. 7 (2008) 442–453, https://doi.org/10.1038/NMAT2162.

[2] M.L. Brongersma, N.J. Halas, P. Nordlander, Plasmon-induced hot carrier science and technology, Nat. Nanotechnol. 10 (1 10) (2015) 25–34, https://doi.org/10.1038/nnano.2014.311, 2015.

[3] H. Chen, L. Shao, Q. Li, J. Wang, Gold nanorods and their plasmonic properties, Chem. Soc. Rev. 42 (2013) 2679–2724, https://doi.org/10.1039/C2CS35367A.

[4] N.J. Halas, S. Lal, W.S. Chang, S. Link, P. Nordlander, Plasmons in strongly coupled metallic nanostructures, Chem. Rev. 111 (2011) 3913–3961, https://doi.org/10.1021/CR200061K.

[5] P.K. Jain, X. Huang, I.H. El-Sayed, M.A. El-Sayed, Noble metals on the nanoscale: optical and photothermal properties and some applications in imaging, sensing, biology, and medicine, Acc. Chem. Res. 41 (2008) 1578–1586, https://doi.org/10.1021/AR7002804.

[6] G.V. Naik, V.M. Shalaev, A. Boltasseva, Alternative plasmonic materials: beyond gold and silver, Adv. Mater. 25 (2013) 3264–3294, https://doi.org/10.1002/ADMA.201205076.

[7] P.R. West, S. Ishii, G.V. Naik, N.K. Emani, V.M. Shalaev, A. Boltasseva, Searching for better plasmonic materials, Laser Photon. Rev. 4 (2010) 795–808, https://doi.org/10.1002/LPOR.200900055.

[8] A. Comin, L. Manna, New materials for tunable plasmonic colloidal nanocrystals, Chem. Soc. Rev. 43 (2014) 3957–3975, https://doi.org/10.1039/C3CS60265F.

[9] K. Manthiram, A.P. Alivisatos, Tunable localized surface plasmon resonances in tungsten oxide nanocrystals, J. Am. Chem. Soc. 134 (2012) 3995–3998, https://doi.org/10.1021/JA211363W.

[10] X. Ye, J. Fei, B.T. Diroll, T. Paik, C.B. Murray, Expanding the spectral tunability of plasmonic resonances in doped metal-oxide nanocrystals through cooperative cation-anion codoping, J. Am. Chem. Soc. 136 (2014) 11680–11686, https://doi.org/10.1021/JA5039903.

[11] M. Kanehara, H. Koike, T. Yoshinaga, T. Teranishi, Indium tin oxide nanoparticles with compositionally tunable surface plasmon resonance frequencies in the near-IR region, J. Am. Chem. Soc. 131 (2009) 17736–17737, https://doi.org/10.1021/JA9064415.

[12] S.D. Lounis, E.L. Runnerstrom, A. Bergerud, D. Nordlund, D.J. Milliron, Influence of dopant distribution on the plasmonic properties of indium tin oxide nanocrystals, J. Am. Chem. Soc. 136 (2014) 7110–7116, https://doi.org/10.1021/JA502541Z.

[13] X.M. Wang, S. Pan, L. Chen, L. Wang, Y.T. Dai, T. Luo, W.W. Li, Biogenic copper selenide nanoparticles for near-infrared photothermal therapy application, ACS Appl. Mater. Interfaces 15 (2023) 27638–27646, https://doi.org/10.1021/ACSAMI.3C03611.

[14] Z. Liu, J. Wang, K. Qiu, X. Liao, T.W. Rees, L. Ji, H. Chao, Fabrication of red blood cell membrane-camouflaged Cu2−xSe nanoparticles for phototherapy in the second near-infrared window, Chem. Commun. 55 (2019) 6523–6526, https://doi.org/10.1039/C9CC03148K.

[15] H. Li, M. Shibuta, T. Yamada, H. Hojo, H.S. Kato, T. Teranishi, M. Sakamoto, Band engineering-tuned localized surface plasmon resonance in diverse-phased Cu2–xSySe1–y nanocrystals, J. Phys. Chem. C 126 (2022) 8107–8112, https://doi.org/10.1021/ACS.JPCC.2C01149.

[16] J. Mou, P. Li, C. Liu, H. Xu, L. Song, J. Wang, K. Zhang, Y. Chen, J. Shi, H. Chen, Ultrasmall Cu2-x S nanodots for highly efficient photoacoustic imaging-guided photothermal therapy, Small 11 (2015) 2275–2283, https://doi.org/10.1002/SMLL.201403249.

[17] Y. Liu, M. Liu, M.T. Swihart, Reversible crystal phase interconversion between covellite CuS and high chalcocite Cu2S nanocrystals, Chem. Mater. 29 (2017) 4783–4791, https://doi.org/10.1021/ACS.CHEMMATER.7B00579.

[18] G. Manna, R. Bose, N. Pradhan, Semiconducting and plasmonic copper phosphide platelets, Angew. Chem. Int. Ed. 52 (2013) 6762–6766, https://doi.org/10.1002/ANIE.201210277.

[19] L. De Trizio, R. Gaspari, G. Bertoni, I. Kriegel, L. Moretti, F. Scotognella, L. Maserati, Y. Zhang, G.C. Messina, M. Prato, S. Marras, A. Cavalli, L. Manna, Cu3- xP nanocrystals as a material platform for near-infrared plasmonics and cation exchange reactions, Chem. Mater. 27 (2015) 1120–1128, https://doi.org/10.1021/CM5044792.

[20] P.K.B. Palomaki, E.M. Miller, N.R. Neale, Control of plasmonic and interband transitions in colloidal indium nitride nanocrystals, J. Am. Chem. Soc. 135 (2013) 14142–14150, https://doi.org/10.1021/JA404599G.

[21] S. Askari, D. Mariotti, J.E. Stehr, J. Benedikt, J. Keraudy, U. Helmersson, Low-loss and tunable localized mid-infrared plasmons in nanocrystals of highly degenerate InN, Nano Lett. 18 (2018) 5681–5687, https://doi.org/10.1021/ACS.NANOLETT.8B02260.

[22] X. Liu, W.C. Law, M. Jeon, X. Wang, M. Liu, C. Kim, P.N. Prasad, M.T. Swihart, Cu2–xSe nanocrystals with localized surface plasmon resonance as sensitive contrast agents for in vivo photoacoustic imaging: demonstration of sentinel lymph node mapping, Adv. Healthcare Mater. 2 (2013) 952–957, https://doi.org/10.1002/ADHM.201200388.

[23] Y. Liu, M. Liu, M.T. Swihart, Plasmonic copper sulfide-based materials: a brief introduction to their synthesis, doping, alloying, and applications, J. Phys. Chem. C 121 (2017) 13435–13447, https://doi.org/10.1021/ACS.JPCC.7B00894.

[24] Y. Wu, C. Wadia, W. Ma, B. Sadtler, A.P. Alivisatos, Synthesis and photovoltaic application of copper(1) sulfide nanocrystals, Nano Lett. 8 (2008) 2345–2350, https://doi.org/10.1021/NL801817D.

[25] M. Basu, A.K. Sinha, M. Pradhan, S. Sarkar, Y. Negishi, Govind, T. Pal, Evolution of hierarchical hexagonal stacked plates of CuS from liquid - liquid interface and its photocatalytic application for oxidative degradation of different dyes under indoor lighting, Environ. Sci. Technol. 44 (2010) 6313–6318, https://doi.org/10.1021/ES101323W.

[26] C.H. Lai, K.W. Huang, J.H. Cheng, C.Y. Lee, B.J. Hwang, L.J. Chen, Direct growth of high-rate capability and high capacity copper sulfide nanowire array cathodes for lithium-ion batteries, J. Mater. Chem. 20 (2010) 6638–6645, https://doi.org/10.1039/C0JM00434K.

[27] P. Roy, S.K. Srivastava, Nanostructured copper sulfides: synthesis, properties and applications, CrystEngComm 17 (2015) 7801–7815, https://doi.org/10.1039/C5CE01304F.

[28] J.M. Luther, P.K. Jain, T. Ewers, A.P. Alivisatos, Localized surface plasmon resonances arising from free carriers in doped quantum dots, Nat. Mater. 10 (5 10) (2011) 361–366, https://doi.org/10.1038/nmat3004, 2011.

[29] W. Van Der Stam, S. Gudjonsdottir, W.H. Evers, A.J. Houtepen, Switching between plasmonic and fluorescent copper sulfide nanocrystals, J. Am. Chem. Soc. 139 (2017) 13208–13217, https://doi.org/10.1021/JACS.7B07788.

[30] Y. Xie, A. Riedinger, M. Prato, A. Casu, A. Genovese, P. Guardia, S. Sottini, C. Sangregorio, K. Miszta, S. Ghosh, T. Pellegrino, L. Manna, Copper sulfide nanocrystals with tunable composition by reduction of covellite nanocrystals with Cu+ ions, J. Am. Chem. Soc. 135 (2013) 17630–17637, https://doi.org/10.1021/JA409754V.

[31] R.M. Córdova-Castro, M. Casavola, M. Van Schilfgaarde, A.V. Krasavin, M. A. Green, D. Richards, A.V. Zayats, Anisotropic plasmonic CuS nanocrystals as a natural electronic material with hyperbolic optical dispersion, ACS Nano 13 (2019) 6550–6560, https://doi.org/10.1021/ACSNANO.9B00282.

[32] Y. Xie, L. Carbone, C. Nobile, V. Grillo, S. D'Agostino, F. Della Sala, C. Giannini, D. Altamura, C. Oelsner, C. Kryschi, P.D. Cozzoli, Metallic-like stoichiometric copper sulfide nanocrystals: phase- and shape-selective synthesis, near-infrared surface plasmon resonance properties, and their modeling, ACS Nano 7 (2013) 7352–7369, https://doi.org/10.1021/nn403035s.

[33] X. Zhuo, Z. Liu, R. Aishajiang, T. Wang, D. Yu, Recent progress of copper-based nanomaterials in tumor-targeted photothermal therapy/photodynamic therapy, Pharmaceutics 15 (2023), https://doi.org/10.3390/PHARMACEUTICS15092293.

[34] W.J. Chan, S. Urandur, H. Li, V.S. Goudar, Recent advances in copper sulfide nanoparticles for phototherapy of bacterial infections and cancer, Nanomedicine 18 (2023) 2185–2204, https://doi.org/10.2217/NNM-2023-0202.

[35] C. Xu, K. Pu, Second near-infrared photothermal materials for combinational nanotheranostics, Chem. Soc. Rev. 50 (2021) 1111–1137, https://doi.org/10.1039/D0CS00664E.

[36] F. Barbero, S. Gul, G. Perrone, I. Fenoglio, Photoresponsive inorganic nanomaterials in oncology, Technol. Cancer Res. Treat. 22 (2023), https://doi.org/10.1177/15330338231192850.

[37] S. Nioka, B. Chance, NIR spectroscopic detection of breast cancer, Technol. Cancer Res. Treat. 4 (2005) 497–512, https://doi.org/10.1177/153303460500400504.

[38] F. Barbero, O.H. Moriones, N.G. Bastús, V. Puntes, Dynamic equilibrium in the cetyltrimethylammonium bromide-Au nanoparticle bilayer, and the consequent impact on the formation of the nanoparticle protein corona, Bioconjug. Chem. (2019) 2917–2930, https://doi.org/10.1021/acs.bioconjchem.9b00624.

[39] X. Zhuo, Z. Liu, R. Aishajiang, T. Wang, D. Yu, Recent progress of copper-based nanomaterials in tumor-targeted photothermal therapy/photodynamic therapy, Pharmaceutics 15 (2023) 2293, https://doi.org/10.3390/PHARMACEUTICS15092293, 2023, Vol. 15, Page 2293.

[40] S. Zhang, S. Peng, Copper-Based biomaterials for anti-tumor therapy: recent advances and perspectives, Acta Biomater. 193 (2025) 107–127, https://doi.org/10.1016/J.ACTBIO.2025.01.014.

[41] R. Hu, Y. Fang, M. Huo, H. Yao, C. Wang, Y. Chen, R. Wu, Ultrasmall Cu2-xS nanodots as photothermal-enhanced Fenton nanocatalysts for synergistic tumor therapy at NIR-II biowindow, Biomaterials 206 (2019) 101–114, https://doi.org/10.1016/J.BIOMATERIALS.2019.03.014.

[42] Z. Xu, N. Rao, C.Y. Tang, C.H. Cheng, W.C. Law, Aqueous phase synthesis of Cu2-xS nanostructures and their photothermal generation study, ACS Omega 4 (2019) 14655–14662, https://doi.org/10.1021/ACSOMEGA.9B02204.

[43] M. Tripathi, A. Sharma, S. Sinharay, A.M. Raichur, Effect of PVP molecular weights on the synthesis of ultrasmall cus nanoflakes: synthesis, properties, and potential application for phototheranostics, ACS Appl. Bio Mater. 7 (2024) 1671–1681, https://doi.org/10.1021/ACSABM.3C01123.

[44] X. Li, Z. Hu, J. Ma, X. Wang, Y. Zhang, W. Wang, Z. Yuan, The systematic evaluation of size-dependent toxicity and multi-time biodistribution of gold nanoparticles, Colloids Surf. B Biointerfaces 167 (2018) 260–266, https://doi.org/10.1016/J.COLSURFB.2018.04.005.

[45] S. Vercellino, I. Kokalari, M. Liz Cantoral, V. Petseva, L. Cursi, F. Casoli, V. Castagnola, L. Boselli, I. Fenoglio, Biological interactions of ferromagnetic iron

oxide–carbon nanohybrids with alveolar epithelial cells, Biomater. Sci. 10 (2022) 3514–3526, https://doi.org/10.1039/D2BM00220E.
[46] M. Zhang, X. Qin, W. Xu, Y. Wang, Y. Song, S. Garg, Y. Luan, Engineering of a dual-modal phototherapeutic nanoplatform for single NIR laser-triggered tumor therapy, J. Colloid Interface Sci. 594 (2021) 493–501, https://doi.org/10.1016/J.JCIS.2021.03.050.
[47] E. Fanizza, R. Mastrogiacomo, O. Pugliese, A. Guglielmelli, L. De Sio, R. Castaldo, M.P. Scavo, M. Giancaspro, F. Rizzi, G. Gentile, F. Vischio, L. Carrieri, I. De Pasquale, G. Mandriota, F. Petronella, C. Ingrosso, M. Lavorgna, R. Comparelli, M. Striccoli, M.L. Curri, N. Depalo, NIR-absorbing mesoporous silica-coated copper sulphide nanostructures for light-to-thermal energy conversion, Nanomaterials 12 (2022), https://doi.org/10.3390/nano12152545.
[48] M. Zhou, J. Li, S. Liang, A.K. Sood, D. Liang, C. Li, CuS nanodots with ultrahigh efficient renal clearance for positron emission tomography imaging and image-guided photothermal therapy, ACS Nano 9 (2015) 7085–7096, https://doi.org/10.1021/ACSNANO.5B02635.
[49] M.R. Kim, H.A. Hafez, X. Chai, L.V. Besteiro, L. Tan, T. Ozaki, A.O. Govorov, R. Izquierdo, D. Ma, Covellite CuS nanocrystals: realizing rapid microwave-assisted synthesis in air and unravelling the disappearance of their plasmon resonance after coupling with carbon nanotubes, Nanoscale 8 (2016) 12946–12957, https://doi.org/10.1039/C6NR03426H.
[50] D.K. Roper, W. Ahn, M. Hoepfner, Microscale heat transfer transduced by surface plasmon resonant gold nanoparticles, J. Phys. Chem. C 111 (2007) 3636–3641, https://doi.org/10.1021/JP064341W.
[51] S. Zhang, C. Sun, J. Zeng, Q. Sun, G. Wang, Y. Wang, Y. Wu, S. Dou, M. Gao, Z. Li, Ambient aqueous synthesis of ultrasmall PEGylated Cu2−xSe nanoparticles as a multifunctional theranostic agent for multimodal imaging guided photothermal therapy of cancer, Adv. Mater. 28 (2016) 8927–8936, https://doi.org/10.1002/ADMA.201602193.
[52] X. Ding, C.H. Liow, M. Zhang, R. Huang, C. Li, H. Shen, M. Liu, Y. Zou, N. Gao, Z. Zhang, Y. Li, Q. Wang, S. Li, J. Jiang, Surface plasmon resonance enhanced light absorption and photothermal therapy in the second near-infrared window, J. Am. Chem. Soc. 136 (2014) 15684–15693, https://doi.org/10.1021/JA508641Z.
[53] K. Mareschi, A.G.S. Banche Niclot, E. Marini, E. Bari, L. Labanca, G. Lucania, I. Ferrero, S. Perteghella, M.L. Torre, F. Fagioli, A new human platelet lysate for mesenchymal stem cell production compliant with good manufacturing practice conditions preserves the chemical characteristics and biological activity of lyo-secretome isolated by ultrafiltration, Int. J. Mol. Sci. 23 (2022), https://doi.org/10.3390/IJMS23084318.
[54] K. Mareschi, S. Castiglia, A. Adamini, D. Rustichelli, E. Marini, A.G.S.B. Niclot, M. Bergallo, L. Labanca, I. Ferrero, F. Fagioli, Inactivated platelet lysate supports the proliferation and immunomodulant characteristics of mesenchymal stromal cells in GMP culture conditions, Biomedicines 8 (2020) 220, https://doi.org/10.3390/BIOMEDICINES8070220, 2020, Vol. 8, Page 220.
[55] B. Pejjai, M. Reddivari, T.R.R. Kotte, Phase controllable synthesis of CuS nanoparticles by chemical co-precipitation method: effect of copper precursors on the properties of CuS, Mater. Chem. Phys. 239 (2020) 122030, https://doi.org/10.1016/J.MATCHEMPHYS.2019.122030.
[56] L. Wang, Synthetic methods of CuS nanoparticles and their applications for imaging and cancer therapy, RSC Adv. 6 (2016) 82596–82615, https://doi.org/10.1039/C6RA18355G.
[57] M. Zhou, R. Zhang, M. Huang, W. Lu, S. Song, M.P. Melancon, M. Tian, D. Liang, C. Li, A chelator-free multifunctional [64Cu]CuS nanoparticle platform for simultaneous micro-PET/CT imaging and photothermal ablation therapy, J. Am. Chem. Soc. 132 (2010) 15351–15358, https://doi.org/10.1021/JA106855M.
[58] Y. Zhao, H. Pan, Y. Lou, X. Qiu, J. Zhu, C. Burda, Plasmonic Cu 2-xS nanocrystals: optical and structural properties of copper-deficient copper(I) sulfides, J. Am. Chem. Soc. 131 (2009) 4253–4261, https://doi.org/10.1021/JA805655B.
[59] M. Adelifard, H. Eshghi, M.M.B. Mohagheghi, An investigation on substrate temperature and copper to sulphur molar ratios on optical and electrical properties of nanostructural CuS thin films prepared by spray pyrolysis method, Appl. Surf. Sci. 258 (2012) 5733–5738, https://doi.org/10.1016/J.APSUSC.2012.02.079.
[60] E. Koushki, H.A. Doost, Optical spectra of conjugated gold nano-colloids; Scattering cross section and effects of solvent and polydispersity, Results Chem. 13 (2025) 102024, https://doi.org/10.1016/J.RECHEM.2025.102024.
[61] J.P. Oliveira, A.R. Prado, W.J. Keijok, M.R.N. Ribeiro, M.J. Pontes, B.V. Nogueira, M.C.C. Guimarães, A helpful method for controlled synthesis of monodisperse gold nanoparticles through response surface modeling, Arab. J. Chem. 13 (2020) 216–226, https://doi.org/10.1016/J.ARABJC.2017.04.003.
[62] B. Sepúlveda, P.C. Angelomé, L.M. Lechuga, L.M. Liz-Marzán, LSPR-based nanobiosensors, Nano Today 4 (2009) 244–251, https://doi.org/10.1016/J.NANTOD.2009.04.001.
[63] S. Link, M.A. El-Sayed, Shape and size dependence of radiative, non-radiative and photothermal properties of gold nanocrystals, Int. Rev. Phys. Chem. 19 (2000) 409–453, https://doi.org/10.1080/01442350050034180.
[64] P. Lukashev, W.R.L. Lambrecht, T. Kotani, M. Van Schilfgaarde, Electronic and crystal structure of Cu2-x S: full-potential electronic structure calculations, Phys. Rev. B Condens. Matter 76 (2007) 195202, https://doi.org/10.1103/PHYSREVB.76.195202.
[65] N.G. Bastús, J. Piella, V. Puntes, Quantifying the sensitivity of multipolar (dipolar, quadrupolar, and octapolar) surface plasmon resonances in silver nanoparticles: the effect of size, composition, and surface coating, Langmuir 32 (2016) 290–300, https://doi.org/10.1021/ACS.LANGMUIR.5B03859.
[66] Y.T. Kwon, G.D. Lim, S. Kim, S.H. Ryu, H.R. Lim, Y.H. Choa, Effect of localized surface plasmon resonance on dispersion stability of copper sulfide nanoparticles, Appl. Surf. Sci. 477 (2019) 204–210, https://doi.org/10.1016/J.APSUSC.2017.11.006.
[67] M. Guzman, M. Arcos, J. Dille, C. Rousse, S. Godet, L. Malet, Effect of the concentration and the type of dispersant on the synthesis of copper oxide nanoparticles and their potential antimicrobial applications, ACS Omega 6 (2021) 18576–18590, https://doi.org/10.1021/ACSOMEGA.1C00818.
[68] M. Shahmiri, N.A. Ibrahim, F. Shayesteh, N. Asim, N. Motallebi, Preparation of PVP-coated copper oxide nanosheets as antibacterial and antifungal agents, J. Mater. Res. 28 (2013) 3109–3118, https://doi.org/10.1557/JMR.2013.316/METRICS.
[69] N. Soltani, E. Saion, M. Erfani, K. Rezaee, G. Bahmanrokh, G.P.C. Drummen, A. Bahrami, M.Z. Hussein, Influence of the polyvinyl pyrrolidone concentration on particle size and dispersion of ZnS nanoparticles synthesized by microwave irradiation, Int. J. Mol. Sci. 13 (2012) 12412–12427, https://doi.org/10.3390/IJMS131012412, 2012, Vol. 13, Pages 12412-12427.
[70] M. Liu, X. Yan, H. Liu, W. Yu, An investigation of the interaction between polyvinylpyrrolidone and metal cations, React. Funct. Polym. 44 (2000) 55–64, https://doi.org/10.1016/S1381-5148(99)00077-2.
[71] G. Granata, A. Onoguchi, C. Tokoro, Preparation of copper nanoparticles for metal-metal bonding by aqueous reduction with d-glucose and PVP, Chem. Eng. Sci. 209 (2019) 115210, https://doi.org/10.1016/J.CES.2019.115210.
[72] N.T.K. Thanh, N. Maclean, S. Mahiddine, Mechanisms of nucleation and growth of nanoparticles in solution, Chem. Rev. 114 (2014) 7610–7630, https://doi.org/10.1021/CR400544S.
[73] S. Shi, X. Wen, T. Li, X. Wen, Q. Cao, X. Liu, Y. Liu, M.D. Pagel, C. Li, Thermosensitive biodegradable copper sulfide nanoparticles for real-time multispectral optoacoustic tomography, ACS Appl. Bio Mater. 2 (2019) 3203–3211, https://doi.org/10.1021/ACSABM.9B00133.
[74] Y. Yin, Y. Xiao, G. Lin, Q. Xiao, Z. Lin, Z. Cai, An enzyme–inorganic hybrid nanoflower based immobilized enzyme reactor with enhanced enzymatic activity, J. Mater. Chem. B 3 (2015) 2295–2300, https://doi.org/10.1039/C4TB01697A.
[75] S.K. Shinde, V.J. Fulari, D.Y. Kim, N.C. Maile, R.R. Koli, H.D. Dhaygude, G. S. Ghodake, Chemical synthesis of flower-like hybrid Cu(OH)2/CuO electrode: application of polyvinyl alcohol and triton X-100 to enhance supercapacitor performance, Colloids Surf. B Biointerfaces 156 (2017) 165–174, https://doi.org/10.1016/J.COLSURFB.2017.05.018.
[76] F. Barbero, E. Destro, A. Bellone, L. Di Lorenzo, V. Brunella, G. Perrone, A. Damin, I. Fenoglio, Hydrothermal carbonization synthesis of amorphous carbon nanoparticles (15–150 nm) with fine-tuning of the size, bulk order, and the consequent impact on antioxidant and photothermal properties, Nanoscale Adv. (2025), https://doi.org/10.1039/D4NA00923A.
[77] I. Kokalari, R. Gassino, A.M. Giovannozzi, L. Croin, E. Gazzano, E. Bergamaschi, A.M. Rossi, G. Perrone, C. Riganti, J. Ponti, I. Fenoglio, Pro- and anti-oxidant properties of near-infrared (NIR) light responsive carbon nanoparticles, Free Radic. Biol. Med. 134 (2019) 165–176, https://doi.org/10.1016/J.FREERADBIOMED.2019.01.013.
[78] I. Kokalari, S. Keshavan, M. Rahman, E. Gazzano, G. Barzan, L. Mandrile, A. Giovannozzi, J. Ponti, G. Antonello, M. Monopoli, G. Perrone, E. Bergamaschi, C. Riganti, B. Fadeel, I. Fenoglio, Efficacy, biocompatibility and degradability of carbon nanoparticles for photothermal therapy of lung cancer, Nanomedicine 16 (2021) 689–707, https://doi.org/10.2217/NNM-2021-0009.
[79] H. Wu, V.W. Or, S. Gonzalez-Calzada, V.H. Grassian, CuS nanoparticles in humid environments: adsorbed water enhances the transformation of CuS to CuSO4, Nanoscale 12 (2020) 19350–19358, https://doi.org/10.1039/D0NR05934J.
[80] B. Li, Y. Xie, Y. Xue, Controllable synthesis of cus nanostructures from self-assembled precursors with biomolecule assistance, J. Phys. Chem. C 111 (2007) 12181–12187, https://doi.org/10.1021/JP070861V.
[81] F. Barbero, E. Destro, A. Bellone, L. Di Lorenzo, V. Brunella, G. Perrone, A. A. Damin, I. Fenoglio, F. Barbero, E. Destro, A. Bellone, L. Di Lorenzo, V. Brunella, G. Perrone, A. Damin, I. Fenoglio, Hydrothermal carbonization synthesis of amorphous carbon nanoparticles (15 – 150 nm) with a fine tuning of the size, bulk order, and the consequent impact on antioxidant and photothermal properties, Nanoscale Adv. (2025), https://doi.org/10.1039/D4NA00923A.
[82] S. Bhattacharjee, DLS and zeta potential - what they are and what they are not? J. Contr. Release 235 (2016) 337–351, https://doi.org/10.1016/J.JCONREL.2016.06.017.
[83] Q.L. Li, Y. Sun, L. Ren, X. Wang, C. Wang, L. Li, Y.W. Yang, X. Yu, J. Yu, Supramolecular nanosystem based on pillararene-capped CuS nanoparticles for targeted chemo-photothermal therapy, ACS Appl. Mater. Interfaces 10 (2018) 29314–29324, https://doi.org/10.1021/ACSAMI.8B09330.
[84] X. Liu, B. Li, F. Fu, K. Xu, R. Zou, Q. Wang, B. Zhang, Z. Chen, J. Hu, Facile synthesis of biocompatible cysteine-coated CuS nanoparticles with high photothermal conversion efficiency for cancer therapy, Dalton Trans. 43 (2014) 11709–11715, https://doi.org/10.1039/C4DT00424H.
[85] W. Yu, N. Yu, Z. Wang, X. Li, C. Song, R. Jiang, P. Geng, M. Li, S. Yin, Z. Chen, Chitosan-mediated green synthesis and folic-acid modification of CuS quantum dots for photoacoustic imaging guided photothermal therapy of tumor, J. Colloid Interface Sci. 555 (2019) 480–488, https://doi.org/10.1016/J.JCIS.2019.08.001.
[86] X. Liu, Q. Ren, F. Fu, R. Zou, Q. Wang, G. Xin, Z. Xiao, X. Huang, Q. Liu, J. Hu, CuS@mSiO2-PEG core–shell nanoparticles as a NIR light responsive drug delivery nanoplatform for efficient chemo-photothermal therapy, Dalton Trans. 44 (2015) 10343–10351, https://doi.org/10.1039/C5DT00198F.
[87] J. He, L. Ai, X. Liu, H. Huang, Y. Li, M. Zhang, Q. Zhao, X. Wang, W. Chen, H. Gu, Plasmonic CuS nanodisk assembly based composite nanocapsules for NIR-laser-

driven synergistic chemo-photothermal cancer therapy, J. Mater. Chem. B 6 (2018) 1035–1043, https://doi.org/10.1039/C7TB02772A.
[88] H. Chen, L. Shao, T. Ming, Z. Sun, C. Zhao, B. Yang, J. Wang, Understanding the photothermal conversion efficiency of gold nanocrystals, Small 6 (2010) 2272–2280, https://doi.org/10.1002/SMLL.201001109.
[89] B. Li, Q. Wang, R. Zou, X. Liu, K. Xu, W. Li, J. Hu, Cu7.2S4 nanocrystals: a novel photothermal agent with a 56.7% photothermal conversion efficiency for photothermal therapy of cancer cells, Nanoscale 6 (2014) 3274–3282, https://doi.org/10.1039/C3NR06242B.
[90] M. Millard, Y. Bernhard, N. Canilho, S. Grandemange, S. Parant, M. Mourer, H. P. Lassalle, A. Pasc, Enhanced stability and photothermal efficiency of Indocyanine Green J-aggregates by nanoformulation with Calix[4]arene for photothermal therapy of cancers, Colloids Surf. B Biointerfaces 230 (2023) 113516, https://doi.org/10.1016/J.COLSURFB.2023.113516.
[91] Z. Zha, X. Yue, Q. Ren, Z. Dai, Uniform polypyrrole nanoparticles with high photothermal conversion efficiency for photothermal ablation of cancer cells, Adv. Mater. 25 (2013) 777–782, https://doi.org/10.1002/ADMA.201202211.
[92] F.C. Fang, Antimicrobial reactive oxygen and nitrogen species: concepts and controversies, Nat. Rev. Microbiol. 10 (2) (2004) 820–832, https://doi.org/10.1038/nrmicro1004, 2004 2.
[93] A. O'Reilly, W. Zhao, S. Wickström, E.S.J. Arnér, R. Kiessling, Reactive oxygen species: janus-faced molecules in the era of modern cancer therapy, J. Immunother. Cancer 12 (2024) e009409, https://doi.org/10.1136/JITC-2024-009409.
[94] S.I. Raj, A. Jaiswal, Nanoscale transformation in CuS Fenton-like catalyst for highly selective and enhanced dye degradation, J. Photochem. Photobiol. Chem. 410 (2021) 113158, https://doi.org/10.1016/J.JPHOTOCHEM.2021.113158.
[95] G. Wu, T. Su, P. Zhou, R. Tang, X. Zhu, J. Wang, M. Chao, L. Fan, H. Yan, P. Ye, Engineering M2 macrophage-derived exosomes modulate activated T cell cuproptosis to promote immune tolerance in rheumatoid arthritis, Biomaterials 315 (2025) 122943.
[96] K. Ge, Z. Bai, J. Wang, Z. Li, F. Gao, S. Liu, L. Zhang, F. Gao, C. Xie, Engineering EVs-mediated mRNA delivery regulates microglia function and alleviates depressive-like behaviors, Adv. Mater. (2025) 2418872.
[97] T. Zhou, Z. Yuan, J. Weng, D. Pei, X. Du, C. He, P. Lai, Challenges and advances in clinical applications of mesenchymal stromal cells, J. Hematol. Oncol. 14 (2021) 1–24, https://doi.org/10.1186/S13045-021-01037-X, 2021 14:1.
[98] I. Ferrero, F. Piccinini, P. Marrazzo, M. Monti, C. Pipino, A.S.G. Banche Niclot, C. F. Proto, E. Ragni, R. Hass, G.M. Stella, P. Berni, A. Ivanovska, K. Mareschi, State of the art and new trends from the second international StemNet meeting, Int. J. Mol. Sci. 25 (2024) 2221, https://doi.org/10.3390/IJMS25042221.
[99] D. Li, Y. Yang, G. Zheng, L. Meng, L. Shang, J. Ren, L. Wang, Y. Bao, The potential of cellular homing behavior in tumor immunotherapy: from basic discoveries to clinical applications of immune, mesenchymal stem, and cancer cell homing, Front. Immunol. 15 (2024) 1495978, https://doi.org/10.3389/FIMMU.2024.1495978.
[100] Y. Shan, M. Zhang, E. Tao, J. Wang, N. Wei, Y. Lu, Q. Liu, K. Hao, F. Zhou, G. Wang, Pharmacokinetic characteristics of mesenchymal stem cells in translational challenges, Signal Transduct. Targeted Ther. 9 (2024) 1–27, https://doi.org/10.1038/s41392-024-01936-8, 2024 9:1.
[101] I. Christodoulou, M. Goulielmaki, A. Kritikos, P. Zoumpourlis, G. Koliakos, V. Zoumpourlis, Suitability of human mesenchymal stem cells derived from fetal umbilical cord (Wharton's Jelly) as an Alternative In Vitro Model for Acute Drug Toxicity Screening, Cells 11 (2022) 1102, https://doi.org/10.3390/CELLS11071102.
[102] I. Burghardt, F. Lüthen, C. Prinz, B. Kreikemeyer, C. Zietz, H.G. Neumann, J. Rychly, A dual function of copper in designing regenerative implants, Biomaterials 44 (2015) 36–44, https://doi.org/10.1016/J.BIOMATERIALS.2014.12.022.
[103] W. Xie, Z. Guo, L. Zhao, Y. Wei, The copper age in cancer treatment: From copper metabolism to cuproptosis, Prog. Mater. Sci. 138 (2023) 101145, https://doi.org/10.1016/J.PMATSCI.2023.101145.
[104] S. Zhang, S. Peng, Copper-Based biomaterials for anti-tumor therapy: Recent advances and perspectives, Acta Biomater. 193 (2025) 107–127, https://doi.org/10.1016/J.ACTBIO.2025.01.014.